Contents lists available at ScienceDirect

International Journal of Mechanical Sciences

journal homepage: www.elsevier.com/locate/ijmecsci

Stress shielding effects in pin-loaded hole contact with clearance using FGM

E. Radi

DISMI - Dipartimento di Scienze e Metodi dell'Ingegneria, Università di Modena e Reggio Emilia, Via G. Amendola 2, I-42122 Reggio Emilia, Italy
En&Tech - Centro di Ricerca Interdipartimentale per la Ricerca Industriale ed il Trasferimento Tecnologico, 42122 Reggio Emilia, Italy

ARTICLE INFO

Keywords:
Functionally graded material
Advancing contact
Analytical solution
Clearance
Stress shielding
Optimal design

ABSTRACT

An analytical solution is presented for the contact problem with clearance between a loaded rigid pin and a circular ring made of functionally graded material (FGM), which is inserted around a hole in an infinite isotropic elastic plane. It is assumed that the elastic shear modulus of the FGM ring varies continuously with the radius according to a power law, while the Poisson's ratio is taken costant. The most general expressions for the stress and displacement fields in polar coordinates are considered, both for the FGM ring and the elastic plane. The frictionless contact conditions yield a set of dual trigonometric series equations that can be reduced to a linear system of infinite equations, then solved by truncation. Due to nonlinearity of the advancing contact problem, an inverse method of solution is employed, namely, the contact stress distribution is derived for a set of contact angle values. The corresponding pin load is then calculated, and a nonlinear pointwise relationship is obtained between the contact angle and the pin load. By properly tuning the variation of the material properties within the ring thickness, the contact angle can be increased. Consequently, more uniform distributions can be achieved for the contact pressure and the hoop stress along radial directions, thereby preventing mechanical failure in many fasteners and bolt connections. To compare the stress distributions in the plate with and without the FGM annular reinforcement around the hole, a new solution is worked out as a particular case for the problem of a rigid circular pin in frictionless quasi-conformal contact with a hole in an isotropic elastic plane, and the stress shielding effect consequent to the introduction of the FGM ring is clearly illustrated. The analytical results are then validated against Finite Element predictions, as well as by verifying the invariance of the sum of the classical *M*-integral, taken along circular contours surrounding the hole, together with an area integral that compensates for the path dependence of the *M*-integral in inhomogeneous elastic materials, showing very good agreement.

1. Introduction

In a pinned connection with clearance, stress concentrations typically take place along the contact region, potentially compromising the integrity of the joint, especially for brittle materials. To enhance the wear resistance and fatigue strength of bearing components, such as cylindrical joints and rivet holes, a machine design methodology that is commonly employed involves the creation of surface-hardened bearing surfaces surrounding the hole [1], utilizing techniques such as carburizing, nitriding, or induction hardening [2]. The objective of these techniques is to create a hard surface layer while preserving the ductility of the core material. This combination enhances the component performance by increasing its wear resistance and durability under high load, reducing friction, and hindering crack initiation and propagation under cyclic loading, thus extending its operational life. However, during the hardening process, this methodology may introduce surface defects or residual stresses, which could have a detrimental effect on fatigue life [3].

A further effective method of enhancing the load-bearing capacity and durability of cylindrical joints consists in the insertion of a reinforced ring, composed of high-strength material, around the hole that is in contact with the pin [4,5]. Based on this technique of hole reinforcement, an innovative procedure has been proposed in [6,7] for the assembly of a safe pin-loaded joint in a holed glass plate. The method involves the introduction of a steel ring that is adhered to the plate by means of a soft resin layer. The ring, which is in direct contact with the loaded pin, allows to mitigate high stress concentrations in the brittle glass plate, while the soft layer smooths the contact pressure distribution along the hole rim in the glass plate. However, the change in material properties at the interface between the ring and its surroundings may result in considerable interface shear stress, which could potentially lead to debonding of the components.

Functionally Graded Materials (FGMs) have the potential to replace or supplement the surface-hardening technique or the insertion of a

E-mail address: enrico.radi@unimore.it.

https://doi.org/10.1016/j.ijmecsci.2025.111048
Received 25 June 2025; Received in revised form 20 October 2025; Accepted 18 November 2025

harder collar in some applications. Indeed, their composition and properties undergo a gradual transition over a specific volume (typically from surface to core). These materials may display a gradual transition from a hard to a soft phase, from a metallic to a ceramic phase, or even a combination of both. The use of FGMs in bearing design entails the customization of material properties, including hardness, wear resistance, and toughness, across the entire component rather than merely on its surface. The integration of different materials in variable proportions throughout the thickness of components enables the development of innovative design methodologies [8–10]. For instance, the incorporation of ceramic phases within the contact region has been proved to enhance wear resistance. The gradual variation of material properties inside the bearing surface leads to a smooth distribution of stress and strain fields, which could reduce the risk of surface crack initiation and propagation compared to traditional surface-hardened methods [11–14]. The stress concentrations that appear along the contact region in cylindrical joints can be efficiently reduced by the introduction of a FGM ring in contact with the loaded pin, whose mechanical properties at the outer rim approach those of the surrounding elastic plane. This expedient can lead to a continuous and more uniform stress distribution, thus enhancing the fatigue life of the joint by increasing its durability under cyclic loading conditions [15,16]. The enhanced performance achieved through the implementation of FGMs leads to a reduction in maintenance requirements and an extension of service intervals, consequently decreasing overall lifecycle costs. In contrast, the fabrication of FGMs necessitates the implementation of advanced manufacturing techniques, including powder metallurgy, additive manufacturing, and other specialized processes to create gradual property variation. This request has the effect of increasing the complexity of the production of FGM components and potentially increasing the cost of the process compared to traditional surface-hardening methods. Therefore, the employment of FGMs in the design of innovative connections presents a series of challenging possibilities. However, a critical evaluation of their efficacy must be conducted on a case-by-case basis, against traditional surface-hardening methods, considering the specific performance requirements, manufacturing capabilities, and cost constraints of the application.

With the advancement of additive manufacturing technologies—such as powder-bed fusion, material extrusion, and sheet lamination—it is now possible to fabricate functionally graded materials (FGMs) with continuously varying Young's modulus across spatial dimensions, typically achieved by appropriately blending different constituent materials [17]. A special case of interest involves cylindrical elastic bodies in which the elastic properties vary radially but remain constant in the tangential direction. Such radial inhomogeneity can arise from various processes, including directional cooling that induces a microstructural gradient [18], phase segregation during centrifugal casting [19,20], and surface modification using laser-based techniques [21]. Radially graded FGMs have been extensively studied in the context of axisymmetric problems, especially for structural components such as tubes, rings, disks [22,23], and curved beams [18,24–26]. Additionally, several analytical studies have investigated the influence of radial inhomogeneity on non-axisymmetric problems [27–33].

The design of loaded pinned joints is a classical non-axisymmetric problem in contact mechanics, since it represents the most common technique for connecting an articulated assembly of mechanical components. In general, the pin is a cylinder with a high modulus of elasticity in contact with the surrounding material, which usually has a lower modulus of elasticity. To ensure a sufficient degree of rotational motion of the joint, the hole is slightly larger than the pin. In this case, clearance exerts a significant influence on the contact pressure distribution, and an excessively large amount may lead to wear, fatigue, and failure over time. Due to clearance, the contact between the pin and hole is confined to a limited part of the hole surface, whose extent is unknown and increases non-linearly with the pin load. For this motivation, this kind of advancing contact problem usually requires advanced numerical techniques [34–36]. From the mathematical perspective, this contact condition yields a mixed boundary value problem with a moving boundary, which can be formulated in terms of dual series or integral equations. To obtain a closed-form analytical solution to the problem, it is customary to assume a frictionless contact condition [37–44]. Indeed, accounting for friction necessitates the implementation of a numerical procedure [45–47,35]. A further simplification frequently adopted in the literature consists in assuming the pin as rigid, if sufficiently stiff with respect to the surrounding material [47–50].

The possibility of reducing the Stress Concentration Factor (SCF) in a hole of an elastic plane using FGMs was initially explored in [51], where a Finite Element analysis of the problem of a FGM plane subjected to far-field uniaxial loading was conducted. It was showed that the SCF can be mitigated by gradually increasing the Young's modulus away from the hole, according to an exponential or power-law grading function. Subsequently, the analytical solution for the SCF around a circular hole in an infinite FGM plane under remote biaxial tension and pure shear loading, was presented in [52], by assuming that the elastic properties vary according to exponential functions. Later, the SCF reduction due to the introduction of a FGM annular ring around a circular hole in an infinite homogeneous plane under remote uniaxial tension was investigated analytically in [53,54]. The stress distributions in a panel with a circular hole under far-field uniaxial loading with the hole rim lined with either a compressible or an incompressible FGM ring were obtained in [55,56], respectively. It was observed that the introduction of the FGM ring reduces both the contact pressure and maximum hoop stress in the panel. Specifically, the SCF can be reduced by about an order of magnitude by appropriately grading Young's modulus in the radial direction, namely by progressively decreasing it towards the hole. Additionally, it was found that it is possible to grade the Young's modulus of the FGM ring to achieve the same SCFs at the hole rim and the interface between the ring and the panel simultaneously. A similar conclusion was provided by the analytical investigation in [57]. The SCF reduction obtained by adopting a linear variation of the Young's modulus with the radius was examined in [23]. A comparative analysis on the SCF reduction caused by the introduction of four different FGM layers around a circular hole in an infinite homogeneous panel was performed in [58] using the extended finite element method (XFEM). It was reported that the power law function is more effective in minimizing SCF, compared to exponential or sigmoid FGMs. The SCF reduction caused by a non-monotonic tri-linear variation of the elastic modulus in an annular FGM inclusion inserted around a circular hole in elastic thin plate and cylindrical shells subject to remote loading was numerically investigated in [59,60] recently, showing that it is possible to reduce the SCF by >50 %. By converting an optimization problem into a nonlinear programming problem, in [61] it was established that a sigmoidal distribution of the Young's modulus around the circular hole allows the hoop stress to attain a minimum value along prescribed radial directions.

From these studies, one can conclude that, although it may not be the optimal solution for reducing the SCF, power-law grading can successfully capture the effects of varying stiffness across the plate, which are important for assessing the contact pressure and SCF near the hole [62]. In particular, the power-law model can be efficiently used when there is a smooth but non-linear variation in material properties. It is often the most practical option for a FGM plate with a hole, because it provides an optimal balance between capturing smooth material transitions and handling the stress concentration effects around the hole. In the special case of unitary grading exponent, it recovers the linear grading model. The latter model is characterized by its simplicity and is applicable when material properties exhibit straight variation [23]. However, it might be too simple and might not adequately capture the complex stress redistribution that occurs around the hole. It may be particularly useful for preliminary analyses. Exponential grading is often chosen to model material variations that initially occur gradually and then change rapidly over a short distance. This model can accurately capture rapid material transitions near the hole, where stress concentrations are of

critical importance. However, the adoption of this model is usually more complex compared to power law grading. Sigmoidal grading models a smooth transition from one material property to another without any abrupt changes. It can be suitable for applications where the material transition occurs gradually, but not as smoothly as a power law. Sigmoidal grading is an excellent choice for simulating smooth and controlled material variations with the ability to fine-tune the transition, especially if the material property change is concentrated around a specific region, such as near the hole edge, without affecting the entire plate. However, the implementation of this model requires careful analysis to ensure numerical stability and to capture the stress distribution accurately. Instead of assuming a specific assigned function for modelling the variation of the material properties, some authors proposed to divide a FGM layer into several sub-layers where the elastic modulus varies linearly, thus approximating an arbitrary function with a piecewise linear one [63,64]. In conclusion, the selection of the grading law depends on the expected material behavior and how accurately stress concentrations and variations in material properties must be captured. In any case, power-law grading is a relatively simple yet effective model that is often a suitable starting point.

The SCF reduction in a pinned joint under non-axisymmetric loading, where the pin is perfectly fit into a hole in an elastic plate with a FGM inter-layer, was investigated in [65]. Since the difference in the elastic moduli of the pin and the plate is responsible for the stress concentration in the softer material, it has been demonstrated that the use of an intermediate FGM layer with a variable Young's modulus, expressed as a power function of the radius, can reduce the gap in rigidity between the joint components and consequently the SCF. Recently, the analytical solution to the frictionless contact problem under clearance-fit conditions between a rigid circular pin and a circular FGM lug with power law grading was obtained in [66]. This study proved that the Hertzian distribution of the contact pressure is valid for very low load levels and a small contact zone, whereas for high loading levels, the contact pressure distribution is almost constant within the central part of the contact zone, and two pressure bumps take place near the ends of the contact zone, whose magnitude decreases as the lug thickness increases thus approaching an almost Hertzian distribution for very thick lugs. Furthermore, it has been demonstrated that the load-bearing capacity of the pin-lug connection can be enhanced by increasing both the elastic modulus and the strength of the FGM lug near the surface in contact with the loaded pin.

To date, no analytical solutions have been published in the technical literature for the contact problem with clearance between a loaded pin and a FGM ring embedded in an infinite elastic plane. In the present work, the plane problem of a loaded rigid pin in advancing contact with a FGM ring inserted around a hole in an isotropic elastic plane is investigated under clearance-fit conditions for the first time. It is assumed that the elastic shear modulus of the FGM ring varies radially according to a power law, continuously approaching that of the surrounding elastic plane. The Poisson ratio is assumed to be constant and equal for both the FGM ring and the elastic plane. In Section 2, the stress and displacement fields in the elastic plane and the FGM ring are represented using a Michell-type series. For the FGM ring in particular, these fields are derived from the solution outlined in [28] for a power-law radial variation of the elastic modulus. Using the frictionless contact boundary conditions, the problem is then reduced to the solution of a set of dual trigonometric series equations. Following the approach developed in [38,66–68], a linear system of infinite equations is derived for the unknown coefficients of the Michell-type series representations and then solved by truncation in Section 3. To compare the stress distributions in the plate with and without the FGM annular reinforcement around the hole, a novel solution to the problem of a rigid circular pin in frictionless quasi-conformal contact with a hole in an isotropic elastic plane is then worked out in Section 4 as a particular case. Results are then presented in Section 5 for the contact angle and the stress components both in the FGM ring and the elastic plane, for various loading levels and geometrical and material parameters. The correctness of the analytical results is verified in Section 6 by exploiting the invariance property of the *M*-integral along circular contours surrounding the hole. First, a combination of the classical *M*-integral for homogeneous elastic solids with an area integral, derived using the Gauss-Green theorem to ensure that the sum of the two integrals remains invariant, is presented in Appendix B. Then, it is shown that substituting the analytical stress and displacement fields into this combination yields a constant value at any distance from the hole. The results are also validated against Finite Element predictions in the Supplementary Material.

The present contribution intends to offer practical suggestions regarding the optimal conditions for enhancing the load-bearing capacity of pinned connections by exploiting the properties of FGMs. Furthermore, this work paves the way for innovative optimization in the design of cylindrical joints, with potentially wide applications.

2. Problem formulation

The problem of a loaded rigid pin in frictionless quasi-conformal contact with a FGM ring embedded in an infinite isotropic elastic plane, illustrated in Fig. 1, is considered. The inner and outer radii of the FGM ring are denoted by r_i and r_o, respectively. The elastic shear modulus μ of the FGM ring displays a power-law radial variation according to the relation

$$\mu = \mu_0 (r/r_o)^m, \tag{2.1}$$

where μ_0 is the shear modulus of the homogeneous elastic plane and m is the grading index.

To perform a fully analytical investigation under plane stress or plane strain loading conditions, we assume that the FGM ring and the elastic plane have the same constant Poisson coefficient ν. We consider a small radial clearance $\delta = r_i - r_p$ between the rigid pin and the FGM ring, where r_p is the pin radius, thus leading to an advancing contact problem. Indeed, the contact length between the two components increases as the load P applied to the pin increases. The variation of the shear modulus along the radial direction is sketched in Fig. 2 for specific positive and negative values of the grading index m.

A cylindrical coordinate system $(0, r, \theta)$ is considered with the origin coinciding with the centre of the FGM ring and the axis $\theta = 0$ laying along the direction of the applied load P (Fig. 1).

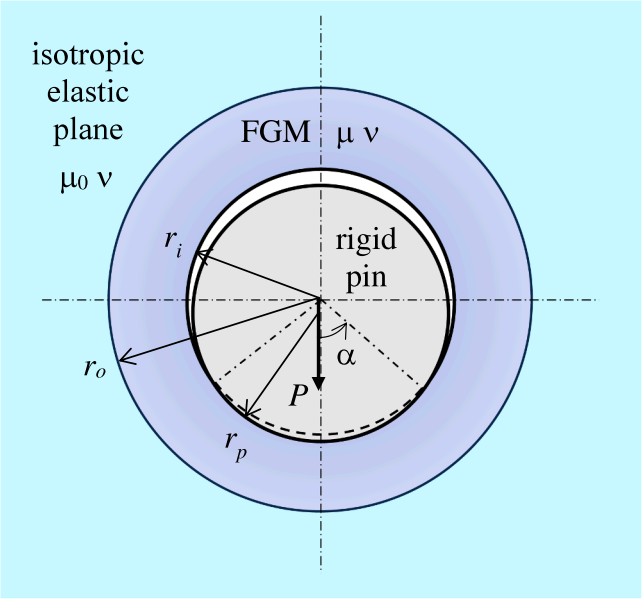

Fig. 1. Loaded rigid pin in a hole in an isotropic elastic plane with a FGM annular reinforcement.

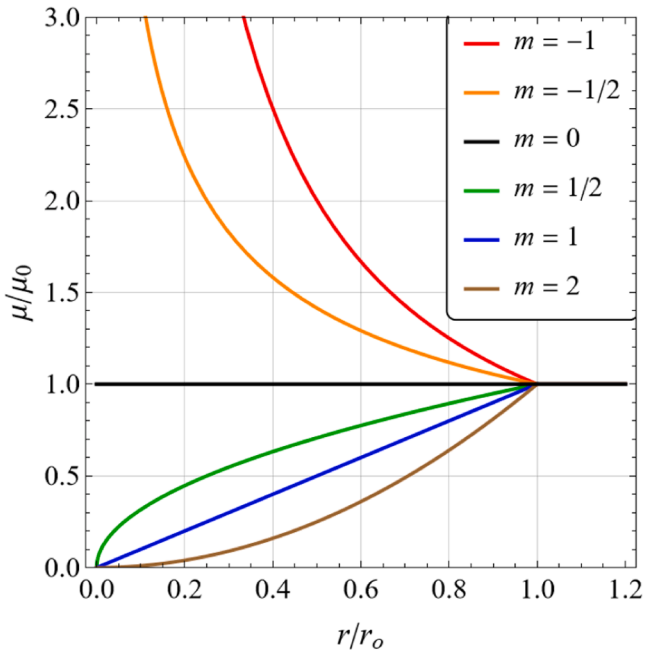

Fig. 2. Variation of the shear modulus along the radial direction for specific values of the grading index m.

The cylindrical components of the stress and displacement fields within the FGM ring, containing only even and single-valued terms in θ, follow from the solution to two-dimensional elastic problems involving graded materials in radial coordinates presented in [28]:

$$\begin{aligned}
\frac{\sigma_{rr}(r,\theta)\ r_o}{2\mu_0\delta} &= \sum_{i=1}^{2}\left[B_{0i}\left(\frac{r}{r_o}\right)^{a_i}+B_{1i}\left(\frac{r}{r_o}\right)^{b_{1i}}\cos\theta\right]+C\frac{r_o}{r}\cos\theta\\
&\quad+\sum_{n=2}^{\infty}\sum_{i=1}^{4}B_{ni}\left(\frac{r}{r_o}\right)^{b_{ni}}\cos n\theta,\\
\frac{\sigma_{\theta\theta}(r,\theta)\ r_o}{2\mu_0\delta} &= \sum_{i=1}^{2}\left[B_{0i}(a_i+1)\left(\frac{r}{r_o}\right)^{a_i}+B_{1i}\left(\frac{r}{r_o}\right)^{b_{1i}}(b_{1i}+2)\cos\theta\right]\\
&\quad+C\Delta\frac{r_o}{r}\cos\theta+\sum_{n=2}^{\infty}\sum_{i=1}^{4}B_{ni}\left(\frac{r}{r_o}\right)^{b_{ni}}(b_{ni}+2)\Delta_{ni}\cos n\theta,\\
\frac{\sigma_{r\theta}(r,\theta)\ r_o}{2\mu_0\delta} &= \left[\sum_{i=1}^{2}B_{1i}\left(\frac{r}{r_o}\right)^{b_{1i}}+C\Delta\frac{r_o}{r}\right]\sin\theta+\sum_{n=2}^{\infty}\sum_{i=1}^{4}B_{ni}\left(\frac{r}{r_o}\right)^{b_{ni}}n\Delta_{ni}\sin n\theta,
\end{aligned}\tag{2.2}$$

$$\begin{aligned}
\frac{u_r(r,\theta)}{\delta} &= \sum_{i=1}^{2}\left[B_{0i}\,\kappa_i\left(\frac{r}{r_o}\right)^{a_i+1-m}+\frac{B_{1i}\,\Gamma_{1i}}{2(1-\rho^2)}\left(\frac{r}{r_o}\right)^{b_{1i}+1-m}\cos\theta\right]\\
&\quad-2C\frac{1+\rho^2+m\rho^2}{m(m+4-2\rho^2)}\left(\frac{r}{r_o}\right)^{-m}\cos\theta+\sum_{n=2}^{\infty}\\
&\quad\times\sum_{i=1}^{4}\frac{B_{ni}\ \chi_{1ni}}{2(1-\rho^2)}\left(\frac{r}{r_o}\right)^{b_{ni}+1-m}\cos n\theta,\\
\frac{u_\theta(r,\theta)}{\delta} &= \left[\sum_{i=1}^{2}\frac{B_{1i}\,\Gamma_{2i}}{2(1-\rho^2)}\left(\frac{r}{r_o}\right)^{b_{1i}+1-m}+2C\frac{1+\rho^2-m+2m\rho^2}{m(m+4-2\rho^2)}\left(\frac{r}{r_o}\right)^{-m}\right]\sin\theta\\
&\quad+\sum_{n=2}^{\infty}\sum_{i=1}^{4}B_{ni}\left(\frac{r}{r_o}\right)^{b_{ni}+1-m}\frac{\chi_{2ni}\sin n\theta}{2n(1-\rho^2)},
\end{aligned}$$

In Eq. (2.2), B_{0i} and B_{1i} (for $i=1,2$), and B_{ni} (for $i=1,2,3,4$ and $n\geq 2$) are arbitrary constants to be determined from the boundary conditions. Moreover:

$$\begin{aligned}
a_{1,2} &= \frac{m}{2}-1\pm\sqrt{\frac{m^2}{4}+2m\rho^2+1-m},\\
b_{11,12} &= \frac{m}{2}-1\pm\sqrt{\frac{m^2}{4}+2m\rho^2+4},\\
\Delta &= \frac{m-2\rho^2(m+1)}{m+4-2\rho^2},\\
\kappa_i &= \frac{1-(1-2\rho^2)(a_i+1)}{2(1-\rho^2)(a_i-m+1)},\\
\Gamma_{1i} &= \frac{1-(b_{1i}+2)(1-2\rho^2)}{b_{1i}-m+1},\\
\Gamma_{2i} &= b_{1i}+1+2\rho^2-\Gamma_{1i},\quad (i=1,2)\\
\Delta_{ni} &= \frac{b_{ni}+1}{b_{ni}-n^2+2},\\
b_{n1,n2} &= \frac{m}{2}-1\pm\sqrt{l_{n1}+\sqrt{l_{n2}}},\\
b_{n3,n4} &= \frac{m}{2}-1\pm\sqrt{l_{n1}-\sqrt{l_{n2}}},\\
l_{n1} &= n^2+\frac{m^2}{4}+m\rho^2+1,\\
l_{n2} &= n^2\left(2+m\rho^2\right)^2-m^2\left(1-\rho^2\right)^2\left(n^2-1\right),\\
\chi_{1ni} &= \frac{1-(b_{ni}+2)(1-2\rho^2)\Delta_{ni}}{b_{ni}-m+1},\\
\chi_{2ni} &= (b_{ni}+2)\Delta_{ni}-1+2\rho^2-\chi_{1ni},\qquad (n=2,3,\ldots;\ i=1,\ldots,4)
\end{aligned}\tag{2.3}$$

where

$$\rho=\sqrt{\frac{1-2\bar{\nu}}{2(1-\bar{\nu})}},\quad \bar{\nu}=\begin{cases}\nu & \text{for plane strain,}\\ \dfrac{\nu}{1+\nu} & \text{for plane stress.}\end{cases}\tag{2.4}$$

Note that a typo occurs in the expression of χ_{2ni} in [28]. The general expressions of the stress and displacement fields in the elastic homogeneous region are given in [69,70]. Considering only the stress terms vanishing at infinity, one has:

$$\begin{aligned}
\frac{\sigma^0_{rr}(r,\theta)\ r_o}{2\mu_0\delta} &= D_0\left(\frac{r_o}{r}\right)^2+\left[D_1\left(2-\rho^2\right)\frac{r_o}{r}-2C_1\left(\frac{r_o}{r}\right)^3\right]\cos\theta\\
&\quad-\sum_{n=2}^{\infty}\left[C_n n(n+1)\left(\frac{r_o}{r}\right)^{n+2}+D_n(n+2)(n-1)\left(\frac{r_o}{r}\right)^{n}\right]\cos n\theta,\\
\frac{\sigma^0_{\theta\theta}(r,\theta)\ r_o}{2\mu_0\delta} &= -D_0\left(\frac{r_o}{r}\right)^2-\left[D_1\rho^2\frac{r_o}{r}-2C_1\left(\frac{r_o}{r}\right)^3\right]\cos\theta\\
&\quad+\sum_{n=2}^{\infty}\left[C_n n(n+1)\left(\frac{r_o}{r}\right)^{n+2}+D_n(n-2)(n-1)\left(\frac{r_o}{r}\right)^{n}\right]\cos n\theta,\\
\frac{\sigma^0_{r\theta}(r,\theta)\ r_o}{2\mu_0\delta} &= -\left[D_1\rho^2\frac{r_o}{r}+2C_1\left(\frac{r_o}{r}\right)^3\right]\sin\theta\\
&\quad-\sum_{n=2}^{\infty}\left[C_n(n+1)\left(\frac{r_o}{r}\right)^{n+2}+D_n(n-1)\left(\frac{r_o}{r}\right)^{n}\right]\sin n\theta,
\end{aligned}\tag{2.5}$$

$$\begin{aligned}\frac{u_r^0(r,\theta)}{\delta} &= -D_0\frac{r_o}{r}+\left\{C_1\left(\frac{r_o}{r}\right)^2+V-D_1\left[(1+\rho^2)\ln\frac{r_o}{r}+\frac{1-\rho^2}{2}\right]\right\}\cos\theta\\ &\quad+\sum_{n=2}^{\infty}\left[C_n n\left(\frac{r_o}{r}\right)^{n+1}+D_n\left(\frac{2\rho^2}{1-\rho^2}+n\right)\left(\frac{r_o}{r}\right)^{n-1}\right]\cos n\theta,\\ \frac{u_\theta^0(r,\theta)}{\delta} &= \left\{C_1\left(\frac{r_o}{r}\right)^2-V+D_1\left[(1+\rho^2)\ln\frac{r_o}{r}-\frac{1-\rho^2}{2}\right]\right\}\sin\theta\\ &\quad+\sum_{n=2}^{\infty}\left[C_n n\left(\frac{r_o}{r}\right)^{n+1}-D_n\left(\frac{2}{1-\rho^2}-n\right)\left(\frac{r_o}{r}\right)^{n-1}\right]\sin n\theta.\end{aligned}$$

The continuity conditions between the elastic homogeneous plane and the outer surface of the FGM ring, at $r=r_o$, require

$$\begin{aligned}&\sigma_{rr}^0(r_o,\theta)=\sigma_{rr}(r_o,\theta),\\ &\sigma_{r\theta}^0(r_o,\theta)=\sigma_{r\theta}(r_o,\theta),\\ &u_r^0(r_o,\theta)=u_r(r_o,\theta),\\ &u_\theta^0(r_o,\theta)=u_\theta(r_o,\theta),\end{aligned}\tag{2.6}$$

for $0\le|\theta|\le\pi$, and the frictionless contact conditions between the rigid pin and the inner surface of the FGM ring, at $r=r_i$ require

$$\begin{aligned}&\sigma_{r\theta}(r_i,\theta)=0, \qquad \text{for} \quad 0\le|\theta|\le\pi,\\ &\sigma_{rr}(r_i,\theta)=0, \qquad \text{for} \quad \alpha\le|\theta|\le\pi,\\ &u_r(r_i,\theta)=v_0\cos\theta-\delta(1-\cos\theta), \qquad \text{for} \quad 0\le|\theta|\le\alpha,\end{aligned}\tag{2.7}$$

where α is the unknown contact angular extent and v_0 denotes a rigid body motion of the pin along the loading direction. The contact condition $(2.7)_3$ was derived and discussed in [34,42,44] for a contact problem between a cylindrical pin and a hole, and it holds for small clearance $\delta << r_i$.

By imposing the boundary conditions (2.6) and $(2.7)_1$, using the stress and displacement fields for the FGM ring (2.2) and for the elastic plane (2.5), one obtains the following relations for the unknown constants that appears in the expressions of the stress and displacement in the elastic plane in terms of the constants B_{ni} ($i=1,2,3,4$; $n=0,1,2,\ldots$) entering the stress and displacement fields in the FGM ring:

$$\begin{aligned}D_0 &= \sum_{i=1}^{2}B_{0i},\\ D_1 &= \frac{\Delta-1}{2\Delta}\sum_{i=1}^{2}\lambda^{b_{1i}+1}B_{1i},\\ C &= -\frac{1}{\Delta}\sum_{i=1}^{2}\lambda^{b_{1i}+1}B_{1i},\\ C_1 &= \frac{1}{2}\sum_{i=1}^{2}\left[\left(1-\frac{\rho^2}{2}+\frac{\rho^2}{2\Delta}\right)\lambda^{b_{1i}+1}-1\right]B_{1i},\\ V &= \frac{1}{2}\sum_{i=1}^{2}\left[1-\frac{\Delta+1}{2\Delta}\lambda^{b_{1i}+1}+\frac{4(1+\rho^2+m\rho^2)\lambda^{b_{1i}+1}}{m(m-2\rho^2-2m\rho^2)}+\frac{\Gamma_{1i}}{1-\rho^2}\right]B_{1i},\\ D_n &= \sum_{i=1}^{4}\frac{n\Delta_{ni}-1}{2(n-1)}B_{ni},\\ C_n &= \sum_{i=1}^{4}\frac{1-\Delta_{ni}(n+2)}{2(n+1)}B_{ni}, \qquad (n=2,3,\ldots)\end{aligned}\tag{2.8}$$

where $\lambda=r_i/r_o<1$ is the FGM ring aspect ratio. Moreover, the following relations are also obtained between constants B_{01} and B_{02}:

$$\sum_{i=1}^{2}(1+\kappa_i)B_{0i}=0,\tag{2.9}$$

between constants B_{11} and B_{12}:

$$\sum_{i=1}^{2}\left[\frac{2m(1-\rho^2)\lambda^{b_{1i}+1}}{m-2\rho^2-2m\rho^2}-\frac{b_{1i}+3}{1-\rho^2}\right]B_{1i}=0,\tag{2.10}$$

and between constants B_{ni} for $i=1,2,3,4$, and $n=0,1,2,\ldots$:

$$\begin{aligned}&\sum_{i=1}^{4}\lambda^{b_{ni}}\Delta_{ni}B_{ni}=0,\\ &\sum_{i=1}^{4}\left[\chi_{1ni}-2\frac{n(1+n\rho^2)\Delta_{ni}-n-\rho^2}{n^2-1}\right]B_{ni}=0,\\ &\sum_{i=1}^{4}\left[\chi_{2ni}+2n\frac{n(n+\rho^2)\Delta_{ni}-1-n\rho^2}{n^2-1}\right]B_{ni}=0.\end{aligned}\tag{2.11}$$

From Eqs. (2.9), (2.10), and (2.11) one can find

$$\begin{aligned}B_{02} &= -B_{01}\frac{1+\kappa_1}{1+\kappa_2},\\ B_{12} &= -\beta B_{11},\\ B_{ni} &= c_{ni}\quad B_{n1},(n=2,3,\ldots;\ i=2,3,4)\end{aligned}\tag{2.12}$$

respectively, where

$$\beta=\frac{2m\lambda^{b_{11}+1}(1-\rho^2)^2-(m-2\rho^2-2m\rho^2)(b_{11}+3)}{2m\lambda^{b_{12}+1}(1-\rho^2)^2-(m-2\rho^2-2m\rho^2)(b_{12}+3)},\tag{2.13}$$

and c_{n2}, c_{n3}, and c_{n4}, for $n\ge2$, can be calculated from the system (2.11) using $(2.12)_3$.

The contact conditions $(2.7)_{2,3}$ then yield the following dual series equations

$$\sum_{i=1}^{2}B_{0i}\lambda^{a_i}+\frac{\Delta-1}{\Delta}\sum_{i=1}^{2}B_{1i}\lambda^{b_{1i}}\cos\theta+\sum_{n=2}^{\infty}\sum_{i=1}^{4}B_{ni}\lambda^{b_{ni}}\cos n\theta=0,$$

for $\alpha\le|\theta|\le\pi$,

$$\begin{aligned}&\sum_{i=1}^{2}B_{0i}\kappa_i\lambda^{a_i}+\sum_{i=1}^{2}B_{1i}\lambda^{b_{1i}}\left[\frac{\Gamma_{1i}}{2(1-\rho^2)}+\frac{2(1+\rho^2+m\rho^2)}{m(m-2\rho^2-2m\rho^2)}\right]\cos\theta\\ &\quad+\sum_{n=2}^{\infty}\sum_{i=1}^{4}B_{ni}\frac{\lambda^{b_{ni}}\chi_{1ni}}{2(1-\rho^2)}\cos n\theta=\left(\frac{\delta+v_0}{\delta}\cos\theta-1\right)\lambda^{m-1},\end{aligned}\tag{2.14}$$

for $0\le|\theta|\le\alpha$.

Using relations (2.12), from Eq. (2.14) one obtains

$$\begin{aligned}&B_{01}\left(\lambda^{a_1}-\lambda^{a_2}\frac{1+\kappa_1}{1+\kappa_2}\right)+B_{11}\frac{\Delta-1}{\Delta}\left(\lambda^{b_{11}}-\beta\lambda^{b_{12}}\right)\cos\theta\\ &\quad+\sum_{n=2}^{\infty}B_{n1}\sum_{i=1}^{4}c_{ni}\lambda^{b_{ni}}\cos n\theta=0, \quad \text{for } \alpha\le|\theta|\le\pi,\\ &B_{01}\left(\kappa_1\lambda^{a_1}-\frac{1+\kappa_1}{1+\kappa_2}\kappa_2\lambda^{a_2}\right)+B_{11}\left[\frac{\lambda^{b_{11}}\Gamma_{11}-\beta\lambda^{b_{12}}\Gamma_{12}}{2(1-\rho^2)}\right.\\ &\quad\left.+\frac{2(1+\rho^2+m\rho^2)\left(\lambda^{b_{11}}-\beta\lambda^{b_{12}}\right)}{m(m-2\rho^2-2m\rho^2)}\right]\cos\theta\\ &\quad+\sum_{n=2}^{\infty}B_{n1}\sum_{i=1}^{4}c_{ni}\frac{\lambda^{b_{ni}}\chi_{1ni}}{2(1-\rho^2)}\cos n\theta=\left(\frac{\delta+v_0}{\delta}\cos\theta-1\right)\lambda^{m-1},\\ &\text{for } 0\le|\theta|\le\alpha,\end{aligned}\tag{2.15}$$

namely:

$$\frac{A_0}{2}+\sum_{n=2}^{\infty}A_n\cos n\theta=0,\quad \text{for } \alpha\le|\theta|\le\pi,$$
$$\frac{A_0}{2}\,\frac{\lambda^{a_1}\kappa_1(1+\kappa_2)-\lambda^{a_2}\kappa_2(1+\kappa_1)}{\lambda^{a_1}(1+\kappa_2)-\lambda^{a_2}(1+\kappa_1)}+\sum_{n=1}^{\infty}\frac{A_n f_n}{1-\rho^2}\cos n\theta \tag{2.16}$$
$$=\left(\frac{\delta+v_0}{\delta}\cos\theta-1\right)\lambda^{m-1},\quad \text{for } 0\le|\theta|\le\alpha,$$

where

$$A_0=2B_{01}\left(\lambda^{a_1}-\lambda^{a_2}\frac{1+\kappa_1}{1+\kappa_2}\right),$$

$$A_1=B_{11}\frac{\Delta-1}{\Delta}\left(\lambda^{b_{11}}-\beta\lambda^{b_{12}}\right), \tag{2.17}$$

$$f_1=\frac{\Delta}{2(\Delta-1)}\left[\frac{\lambda^{b_{11}}\Gamma_{11}-\beta\lambda^{b_{12}}\Gamma_{12}}{\lambda^{b_{11}}-\beta\lambda^{b_{12}}}+\frac{4(1-\rho^2)(1+\rho^2+m\rho^2)}{m\,(m-2\rho^2-2m\rho^2)}\right],$$

and

$$A_n=B_{n1}\sum_{i=1}^{4}c_{ni}\lambda^{b_{ni}},$$
$$f_n=\frac{1}{2}\left(\sum_{i=1}^{4}c_{ni}\lambda^{b_{ni}}\chi_{1ni}\right)\Big/\left(\sum_{j=1}^{4}c_{nj}\lambda^{b_{nj}}\right),\ (n=2,3,\cdots). \tag{2.18}$$

To remove the rigid body displacement v_0, we apply on Eq. (2.16)$_2$ the operator

$$L[\phi]=\frac{\mathrm{d}\phi}{\mathrm{d}\theta}+\int_0^{\theta}\phi(s)\,\mathrm{d}s, \tag{2.19}$$

as suggested in [71,72], thus obtaining

$$\left[\lambda^{m-1}+\frac{A_0}{2}\,\frac{\lambda^{a_1}\kappa_1(1+\kappa_2)-\lambda^{a_2}\kappa_2(1+\kappa_1)}{\lambda^{a_1}(1+\kappa_2)-\lambda^{a_2}(1+\kappa_1)}\right](1-\rho^2)\theta$$
$$-\sum_{n=1}^{\infty}A_n f_n\frac{n^2-1}{n}\sin n\theta=0, \tag{2.20}$$

for $0\le|\theta|\le\alpha$. Then, we apply the procedure used in [66–68] for solving a set of dual series equations similar to Eqs. (2.16)$_1$ and (2.20). To this aim, we rearrange Eq. (2.20) in the form

$$\sum_{n=1}^{\infty}A_n\sin n\theta=(cA_0+d)\theta+\sum_{n=1}^{\infty}h_n A_n\sin n\theta,\quad \text{for } 0\le|\theta|\le\alpha, \tag{2.21}$$

where

$$\begin{aligned}c &= -\frac{\lambda^{a_1}\kappa_1(1+\kappa_2)-\lambda^{a_2}\kappa_2(1+\kappa_1)}{2[\lambda^{a_1}(1+\kappa_2)-\lambda^{a_2}(1+\kappa_1)]}(1-\rho^2)\\ d &= -(1-\rho^2)\,\lambda^{m-1},\\ h_n &= 1+\frac{n^2-1}{n}f_n.\end{aligned} \tag{2.22}$$

It is possible to check that

$$f_n=-\frac{1}{n}+\frac{3m-2\rho^2(m+1)}{2n^2}+o(n^{-2}),\quad \text{as } n\to\infty, \tag{2.23}$$

and thus $h_n=O(n^{-1})$ as $n\to\infty$. The latter asymptotic behavior is required for the convergence of the solution to Eq. (2.21). The set of dual Eqs. (2.16)$_1$ and (2.21) can be solved by using the procedure presented in [73], developed in [38], used in [67] and recently adopted in [66,68,74], which yields the following relations for the coefficients A_n, for $n=0, 1, 2,\ldots$:

$$A_0=-4\,(cA_0+d)\ln\left(\cos\frac{\alpha}{2}\right)+\sum_{n=1}^{\infty}n\,h_n A_n J_n, \tag{2.24}$$

$$A_n=(cA_0+d)J_n+\frac{1}{2}\sum_{j=1}^{\infty}jK_{nj}h_j A_j,\qquad (n=1,2,\ldots) \tag{2.25}$$

where [38]:

$$J_n=\frac{1}{n}[P_{n-1}(\cos\alpha)-P_n(\cos\alpha)], \tag{2.26}$$

$$\begin{aligned}K_{nj} &= \frac{(1+\cos\alpha)\sin^2\alpha}{2(n^2-j^2)}[(n+1)P_{j-1}^{(0,1)}(\cos\alpha)P_{n-2}^{(1,2)}(\cos\alpha)\\ &\quad -(j+1)P_{n-1}^{(0,1)}(\cos\alpha)P_{j-2}^{(1,2)}(\cos\alpha)],\end{aligned} \tag{2.27}$$

and $P_n(t)$ and $P_n^{(a,b)}(t)$ denote the Legendre and Jacobi polynomials of order n, respectively. Note also that $J_n\to 0$ as $n\to\infty$.

The results provided in Section 3 in [75] have been used in calculating the integrals (2.26) and (2.27) together with Eq. (3.3) reported in [76]. A detailed derivation of the result (2.27) is illustrated in Appendix B in [68]. Note that for $j=n$, the coefficient K_{nn} in (2.27) is undetermined and thus it must be calculated as a limit [68], namely

$$K_{nn}=\frac{(1+\cos\alpha)\sin^2\alpha}{4n}\Big\{P_{n-1}^{(0,1)}(\cos\alpha)P_{n-2}^{(1,2)}(\cos\alpha)+(n+1)\times$$
$$\left[P_{n-1}^{(0,1)}(\cos\alpha)\frac{d}{dn}P_{n-2}^{(1,2)}(\cos\alpha)-P_{n-2}^{(1,2)}(\cos\alpha)\frac{d}{dn}P_{n-1}^{(0,1)}(\cos\alpha)\right]\Big\}. \tag{2.28}$$

The resultant of the contact pressure distribution must be equal to the total load P applied to the pin, namely

$$P=-2r_i\int_0^{\alpha}\sigma_{rr}(r_i,\theta)\cos\theta\,\mathrm{d}\theta. \tag{2.29}$$

By using Eq. (2.2), (2.12), (2.17), and (2.18), then Eq. (2.29) yields

$$P=-4\mu_0\,\delta\lambda\int_0^{\alpha}\left(\frac{A_0}{2}+\sum_{n=1}^{\infty}A_n\cos n\theta\right)\cos\theta\,\mathrm{d}\theta. \tag{2.30}$$

By calculating the definite integral in (2.30), the load P becomes

$$P=-4\mu_0\delta\lambda\left[\frac{A_0}{2}\sin\alpha+\frac{A_1}{2}\left(\alpha+\frac{\sin 2\alpha}{2}\right)+\sum_{n=2}^{\infty}A_n\frac{n\cos\alpha\sin n\alpha-\sin\alpha\cos n\alpha}{n^2-1}\right]. \tag{2.31}$$

The rigid body motion of the pin follows from Eq. (2.16)$_2$ for $\theta=0$ as

$$v_0=\delta\lambda^{1-m}\left[\frac{A_0}{2}\,\frac{\lambda^{a_1}\kappa_1(1+\kappa_2)-\lambda^{a_2}\kappa_2(1+\kappa_1)}{\lambda^{a_1}(1+\kappa_2)-\lambda^{a_2}(1+\kappa_1)}+\sum_{n=1}^{\infty}\frac{A_n f_n}{1-\rho^2}\right]. \tag{2.32}$$

3. Approximate solution

An approximated solution of the system of infinite algebraic Eqs. (2.24) and (2.25) for the unknown coefficients A_n can be obtained by truncation if a sufficiently large number of terms N is considered, namely:

$$A_0=-4(cA_0+d)\ln\left(\cos\frac{\alpha}{2}\right)+\sum_{n=1}^{N}n\,h_n\,A_n\,J_n, \tag{3.1}$$

$$A_n=(cA_0+d)J_n+\frac{1}{2}\sum_{j=1}^{N}j\,K_{nj}\,h_j\,A_j,\quad (n=1,2,\ldots,N). \tag{3.2}$$

Once the coefficients A_n, for $n=0, 1, 2, \ldots, N$ have been obtained, then an additional number M of coefficients can be calculated by using the following approximate relations

$$A_n=(cA_0+d)J_n+\frac{1}{2}\sum_{j=1}^{n-1}j\,K_{nj}\,h_j\,A_j,\quad (n=N+1,N+2,\ldots,M), \tag{3.3}$$

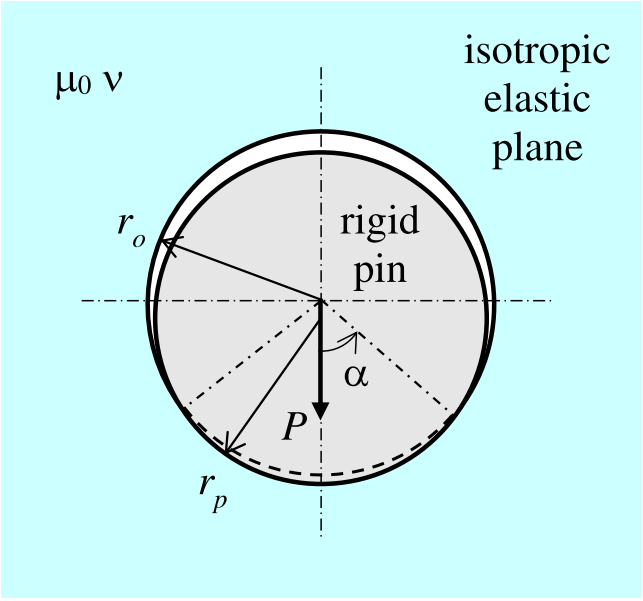

Fig. 3. Geometry and loading of the rigid pin in a hole in an isotropic elastic plane.

which hold based on the decaying behavior of the terms h_n and J_n for large n.

A discrete inverse procedure is then applied to calculate the relation between the load P applied to the pin and the contact half-angle α. An increasing value of α is considered at each step and correspondingly the first $M+1$ unknown coefficients are calculated from the solution to the linear system of Eqs. (3.1) - (3.3). Then, the total load P acting on the pin that causes an angular contact extent of 2α is derived from the relation (2.31).

4. Loaded pin in a hole in an isotropic elastic plate

The problem of a loaded rigid pin of radius r_p in frictionless quasi-conformal contact in a hole in an infinite elastic plane, illustrated in Fig. 3, is considered here as a special case of the approach developed in Sections 2 and 3 in the limit as $m \to 0$. Let r_o, μ_0, and ν denote the hole radius, the shear modulus, and the Poisson coefficient of the isotropic elastic plane, respectively. Let $\delta = r_o - r_p$ be the small radial clearance between the rigid pin and the hole.

The stress and displacement field within the isotropic elastic plate are assumed in the form (2.5), where no rigid motion of the plate is assumed, namely $V = 0$. Then, the frictionless contact conditions between the rigid pin and the hole surface, at $r = r_0$ require

$$\begin{aligned} &\sigma^0_{r\theta}(r_o,\theta) = 0, \qquad \text{for} \quad 0 \le |\theta| \le \pi, \\ &\sigma^0_{rr}(r_o,\theta) = 0, \qquad \text{for} \quad \alpha \le |\theta| \le \pi, \\ &u^0_r(r_o,\theta) = v_0\cos\theta - \delta(1-\cos\theta), \qquad \text{for} \quad 0 \le |\theta| \le \alpha, \end{aligned} \tag{4.1}$$

where α is the unknown contact angular extent and v_0 denotes the rigid body motion of the pin along the loading direction.

By imposing the boundary conditions $(4.1)_1$, one obtains the following relations for the unknown constants that appears in the fields (2.5):

$$C_1 = -\frac{\rho^2}{2}D_1, \qquad C_n = -\frac{n-1}{n+1}D_n. \tag{4.2}$$

The contact conditions $(4.1)_{2,3}$ then yield the following dual series equations

$$\frac{D_0}{2} + D_1\cos\theta - \sum_{n=2}^{\infty} D_n(n-1)\cos n\theta = 0, \quad \text{for } \alpha \le |\theta| \le \pi, \tag{4.3}$$

$$\begin{aligned} &1 - D_0 - \frac{D_1}{2}\cos\theta + 2\sum_{n=2}^{\infty} D_n\left(\frac{1}{1-\rho^2} - \frac{1}{n+1}\right)\cos n\theta \\ &\quad = \left(1 + \frac{v_0}{\delta}\right)\cos\theta, \ \text{for } 0 \le |\theta| \le \alpha, \end{aligned} \tag{4.4}$$

Applying the operator L defined in Eq. (2.19) to Eq. (4.4) in order to remove the rigid body displacement v_0, from Eq. (4.3) and (4.4) one has

$$\frac{A_0}{2} + A_1\cos\theta + \sum_{n=2}^{\infty} A_n\cos n\theta = 0, \quad \text{for } \alpha \le |\theta| \le \pi, \tag{4.5}$$

$$\frac{1-\rho^2}{2}(1-A_0)\theta + \sum_{n=2}^{\infty} A_n\left(1 + \frac{\rho^2}{n}\right)\sin n\theta = 0, \quad \text{for } 0 \le |\theta| \le \alpha, \tag{4.6}$$

where

$$\begin{aligned} A_0 &= D_0, \\ A_1 &= D_1, \\ A_n &= -(n-1)D_n, \quad (n = 2, 3, \ldots). \end{aligned} \tag{4.7}$$

Finally, Eq. (4.6) can be rewritten in the form

$$\sum_{n=1}^{\infty} A_n\sin n\theta = -\frac{1-\rho^2}{2}(1-A_0)\theta - \rho^2\sum_{n=1}^{\infty}\frac{A_n}{n}\sin n\theta = 0, \quad \text{for } 0 \le |\theta| \le \alpha, \tag{4.8}$$

The set of dual Eqs. (4.5) and (4.8) can be solved by using the procedure employed in Sections 2 and 3, which yields the following relations for the coefficients A_n, for $n = 0, 1, 2, \ldots$:

$$A_0 = 2(1-\rho^2)(1-A_0)\ln\left(\cos\frac{\alpha}{2}\right) - \rho^2\sum_{n=1}^{\infty} A_n J_n, \tag{4.9}$$

$$A_n = -\frac{1-\rho^2}{2}(1-A_0)J_n - \frac{\rho^2}{2}\sum_{j=1}^{\infty} K_{nj}A_j, \quad (n = 1, 2, \ldots), \tag{4.10}$$

where J_n and K_{nj} are defined in (2.26) and (2.27). An approximate solution of the system of infinite algebraic Eqs. (4.9) and (4.10) for the unknown coefficients A_n, for $n = 0, 1, 2, \ldots, N$, can be obtained by truncation if a sufficiently large number of terms N is considered. Once the first $N+1$ unknown coefficients A_n, have been calculated, then the pin load P is given by

$$P = -4\mu_0\delta\left[A_0\sin\alpha + A_1\left(\alpha + \frac{\sin 2\alpha}{2}\right) + \sum_{n=2}^{N} 2A_n\frac{n\cos\alpha\sin n\alpha - \sin\alpha\cos n\alpha}{n^2-1}\right]. \tag{4.11}$$

According to Eq. (4.4) for θ = 0 and using Eq. (4.7), the rigid body displacement of the pin is

$$v_0 = -\delta\left[A_0 + \frac{A_1}{2} + \sum_{n=2}^{N}\frac{2A_n}{n-1}\left(\frac{1}{1-\rho^2} - \frac{1}{n+1}\right)\right]. \tag{4.12}$$

5. Results

The main objective of this study is to investigate which type of FGM reinforcement can be used to reduce the stress concentration factor in a pinned connection with clearance. For illustrative purposes, a uniform Poisson's ratio $\nu = 0.3$ is assumed both for the elastic plate and the FGM ring. Initially, the plane strain condition is taken into consideration, and then the plane stress condition is briefly addressed in Sect. 5.1. The stress and displacement fields in the FGM ring and in the infinite isotropic elastic plane are obtained by considering a set of values of the contact half-angle α and then calculating the corresponding resultant

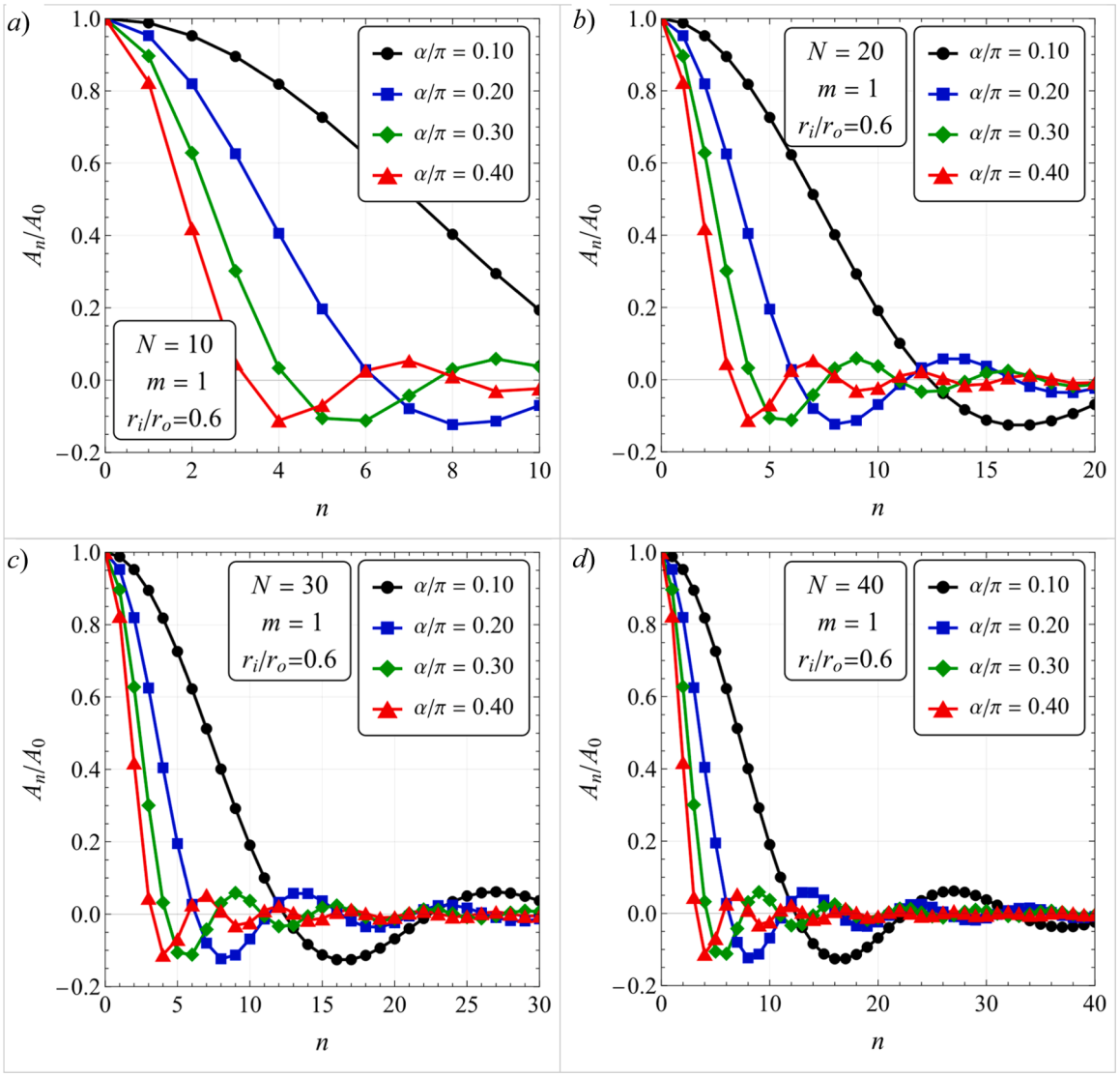

Fig. 4. Variations of the ratios A_n/A_0 for $N = 10$ (*a*), $N = 20$ (*b*), $N = 39$ (*c*), $N = 40$ (*d*), for $m = 1$, $\lambda = 0.6$, and for various values of the contact angle α.

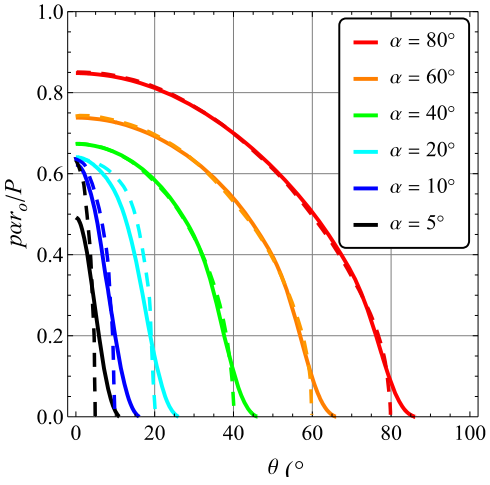

Fig. 5. Contact pressure distribution predicted by the present model for a rigid pin (solid lines) and by the analytical model proposed by Hou and Hills [22] for a ratio between the elastic moduli of the pin and the holed plane equal to 3.

load applied to the pin. To achieve an adequate degree of accuracy in the results, $N \geq 40$ terms are taken for the truncated system (3.1)-(3.2).

The convergence of the series expansion is illustrated in Fig. 4, which shows the variation of the ratios A_n/A_0 (for $0 \leq n \leq N$) as the number of terms increases ($N = 10$, 20, 30, 40), with $m = 1$, $\lambda = 0.6$, and various contact region extents. As the number of terms N increases, the higher-order terms A_n become negligible compared to the leading term A_0, particularly for larger contact regions. It can be observed that a large number of terms is required to obtain a sufficiently accurate solution only when the contact region is very small, a scenario of limited practical relevance. The convergence improves with increasing contact angle, likely due to the assumption of conformal contact embedded in Eq. $(2.7)_3$. Similar convergence trends are observed also for various values of the material and geometric parameters m and λ, thus denoting that convergence requirements are primarily dictated by the extent of the contact region. The results plotted in Fig. 4 thus show the appropriateness to truncate the system (3.1)-(3.2) to the first 40 terms for a contact angular extent $\alpha \geq 0.1\ \pi$.

To mitigate the occurrence of oscillations in the plots due to the Gibbs phenomenon, the Lanczos sigma factors [77] have been introduced in the trigonometric series expansion of the stress and displacement fields.

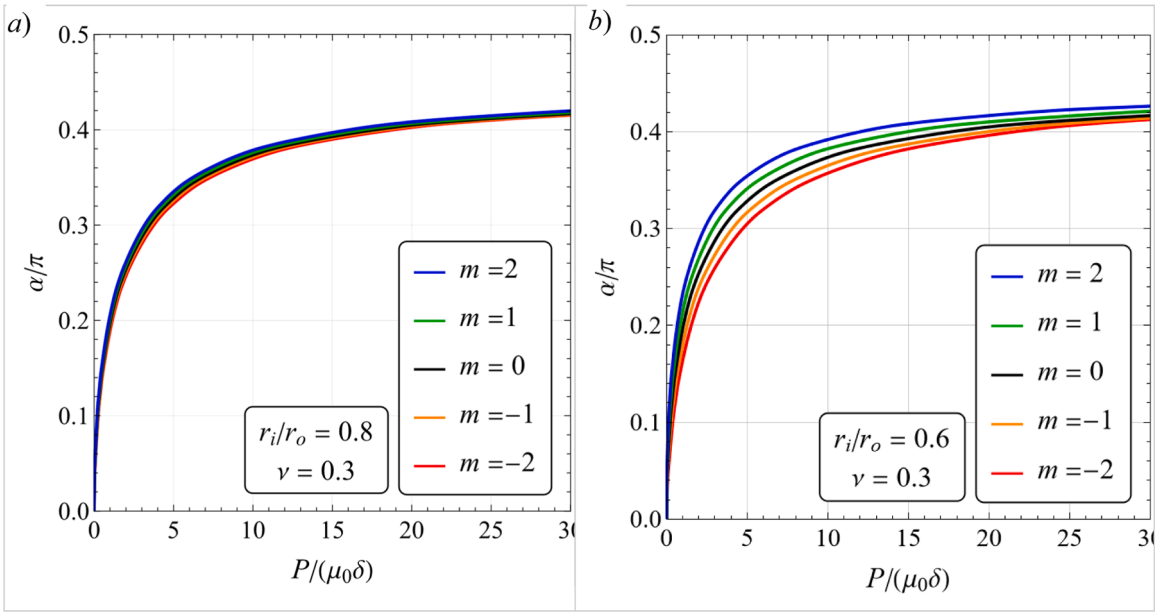

Fig. 6. Normalized variations of the contact half-angle α with the pin load P under plane strain condition for specific values of the grading index m, for a thin FGM ring with $r_i/r_o = 0.8$ (*a*), and a thicker FGM ring with $r_i/r_o = 0.6$ (*b*).

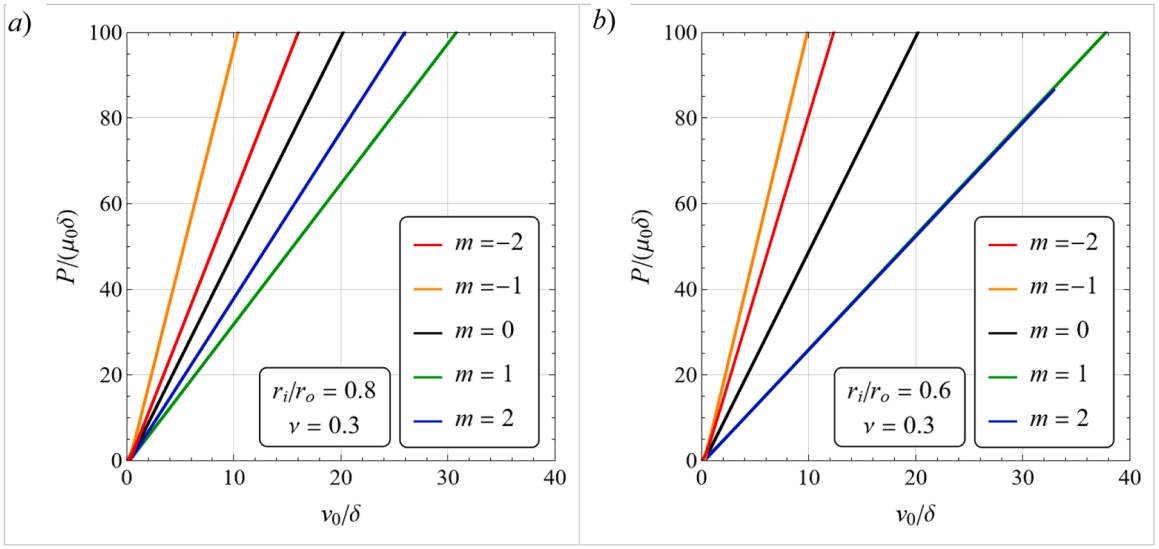

Fig. 7. Normalized variations of the pin load P with the rigid pin displacement for specific values of the grading index m, for a thin FGM ring with $r_i/r_o = 0.8$ (*a*), and a thicker FGM ring with $r_i/r_o = 0.6$ (*b*).

The effects of the clearance amount, grading of material properties, and geometry on the stress fields are assessed by varying the grading index m and the aspect ratio $\lambda = r_i/r_o$ of the FGM ring. As m tends to 0, the special case of uniform shear modulus presented in Section 4 is recovered. In this case, the predictions of the present approach are consistent with those for a rigid pin in a hole in a homogeneous elastic plane provided in [38,41,71]. Moreover, the approach proposed here is validated against previous analytical results available in the literature [44] for the particular case of $m = 0$, as reported in Fig. 5.

The normalized variations of the contact half-angle α with the pin load factor $P/(\mu_0\delta)$ under plane strain conditions are plotted in Figs. 6*a, b*, for specific values of the grading index m, both for a thin FGM ring with $r_i/r_o = 0.8$ (Fig. 6*a*), and a thicker one with $r_i/r_o = 0.6$ (Fig. 6*b*). As the pin load P increases or the clearance δ decreases, the contact half-angle increases non-linearly and approaches a limit value lower than $\pi/2$. In the absence of the FGM ring, it is known that the theoretical maximum contact half-angle is approximately 84°, namely 0.467π [44]. The contact angle also increases as the grading index m increases, namely as the elastic modulus of the FGM ring decreases moving from the outer to the inner rim (see Fig. 2), so that the inner part of the ring becomes softer. Indeed, for a positive grading index, the elastic shear modulus increases within the FGM ring moving from the surface in contact with the pin towards the interface with the elastic plane. There, it reaches the same value μ_0 as the infinite elastic plane (see Fig. 2). An increase in the contact angle then implies a corresponding reduction in the contact pressure.

In general, a lower elastic stiffness of the FGM ring close to the contact surface also implies a larger reduction of the material strength just where the highest stress concentration occurs. Therefore, the load-bearing capacity of the FGM ring with a positive grading index depends on these two effects: a reduction in the stress concentration factor and an associated reduction in the material strength.

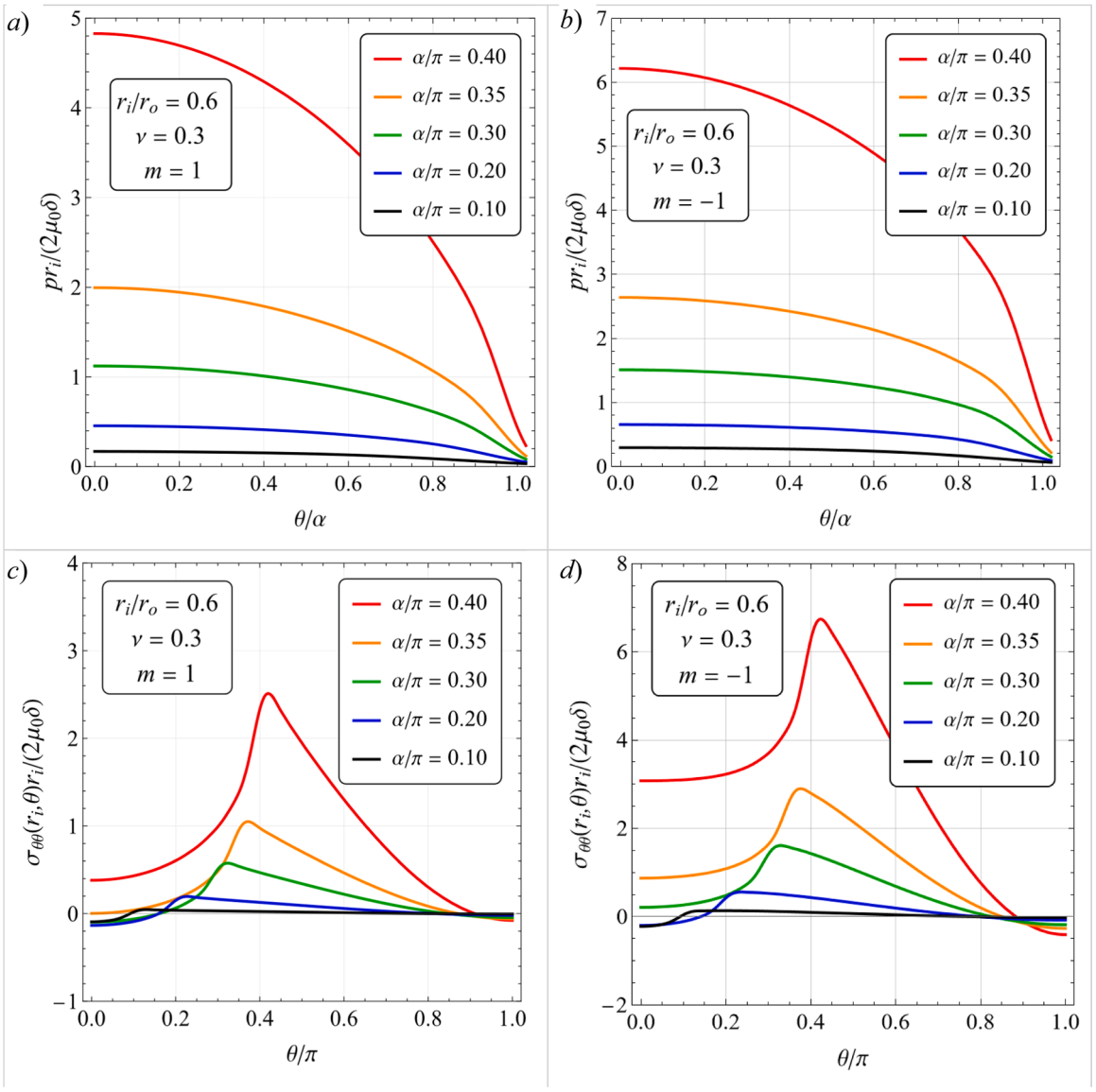

Fig. 8. Normalized variations of the contact pressure (*a, b*) and hoop stress (*c, d*) at the inner rim of the FGM ring (at $r = r_i$) with the angular coordinate θ, for a positive grading index $m = 1$ (*a, c*) and a negative grading index $m = -1$ (*b, d*), for the aspect ratio $r_i/r_o = 0.6$ and various contact angles.

The normalized relations between the pin load and the pin displacement are plotted in Fig. 7 for the same set of values of the grading index m and aspect ratio r_i/r_o considered in Fig. 6. These variations are almost linear, even though the advancing contact problem is non-linear, in agreement with the findings of the FEM investigations in [35]. Furthermore, the same load causes a greater pin displacement for positive grading indices than for negative ones. However, the slope of these plots does not vary monotonically with the grading index m.

The variations of the contact pressure p along the contact surface between a rigid pin and a FGM ring with $r_i/r_o = 0.6$, normalized by the constant shear modulus μ_0 of the outer elastic plane, are plotted in Figs. 8*a,b*, for various contact angles, for positive and negative grading indices ($m = 1$ and $m = -1$, respectively). Unlike the contact problem between a rigid pin and a FGM lug, where the contact pressure distribution displays two symmetrical bumps near the endpoints of the contact region [66,68], the contact pressure distribution for this problem is almost Hertzian, thus it vanishes at the ends of the contact region, and attains a maximum at the centre of the contact region, i.e. at $\theta = 0$. This trend was also observed for a rigid pin in a hole in an elastic isotropic plane [41,49], as well as for the contact problem between two deformable cylindrical solids with FGM coatings with exponential variation of the elastic moduli [78]. Under the same contact angular extent, for $r_i/r_o = 0.6$, the maximum contact pressure for $m = -1$ is about 1.3 times higher than that for $m = 1$. A similar relation holds also between the pin loads P that cause the same contact angular extent for $m = -1$ and $m = 1$.

As already observed, the FGM strength varies with the local shear modulus, and it is expected to increase with the local shear modulus of the FGM [13], meaning that FGM rings with $m < 0$ are expected to be stronger than those with $m > 0$, if the basic shear modulus μ_0 is the same. Therefore, a straight comparison between Figs. 8*a* and 8*b* is not meaningful, as these results occur under different pin loads that cause the same contact angles for $m = 1$ and $m = -1$, according to the results in Fig. 6.

The normalized variations of the hoop stress $\sigma_{\theta\theta}$ along the inner surface of a FGM ring with $r_i/r_o = 0.6$ are plotted in Figs. 8*c,d*, for various contact angles and for $m = 1$ and $m = -1$, respectively. This stress component may be responsible for the formation and propagation of radial cracks under the contact region where it attains its maximum value. The hoop stress displays a finite maximum at an angular coordinate θ slightly larger than the contact half-angle, whose magnitude increases with the pin load. For $r_i/r_o = 0.6$, the maximum hoop stress for

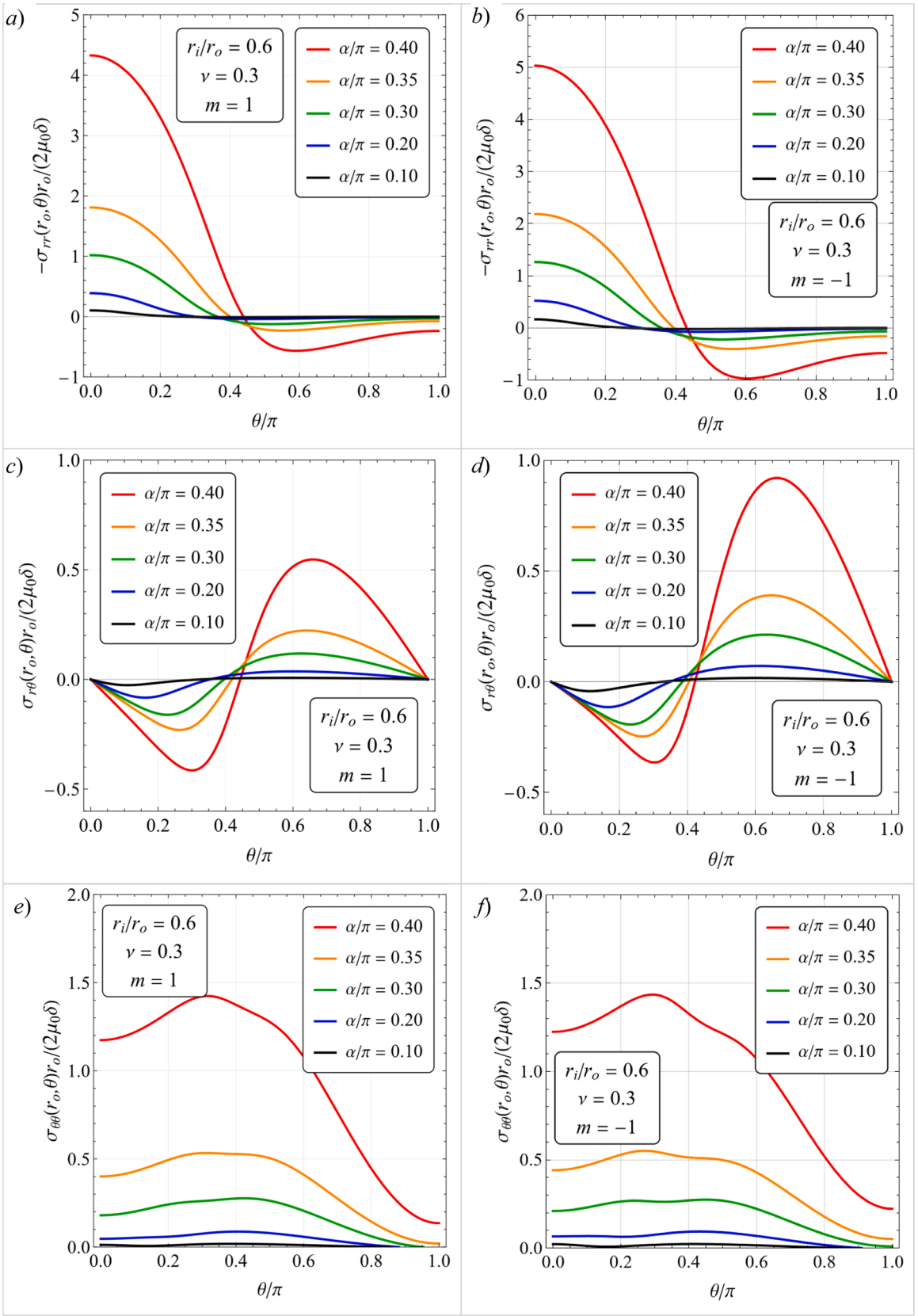

Fig. 9. Normalized variations of the radial (*a, b*), shear (*c, d*), and hoop (*e, f*) stresses along the interface between the FGM ring and the outer elastic plane (at $r = r_o$) with the angular coordinate θ, for various contact angles, for a positive grading index, $m = 1$ (*a, c, e*), and a negative one, $m = -1$ (*b, d, f*), for the aspect ratio $r_i/r_o = 0.6$ and various contact angles.

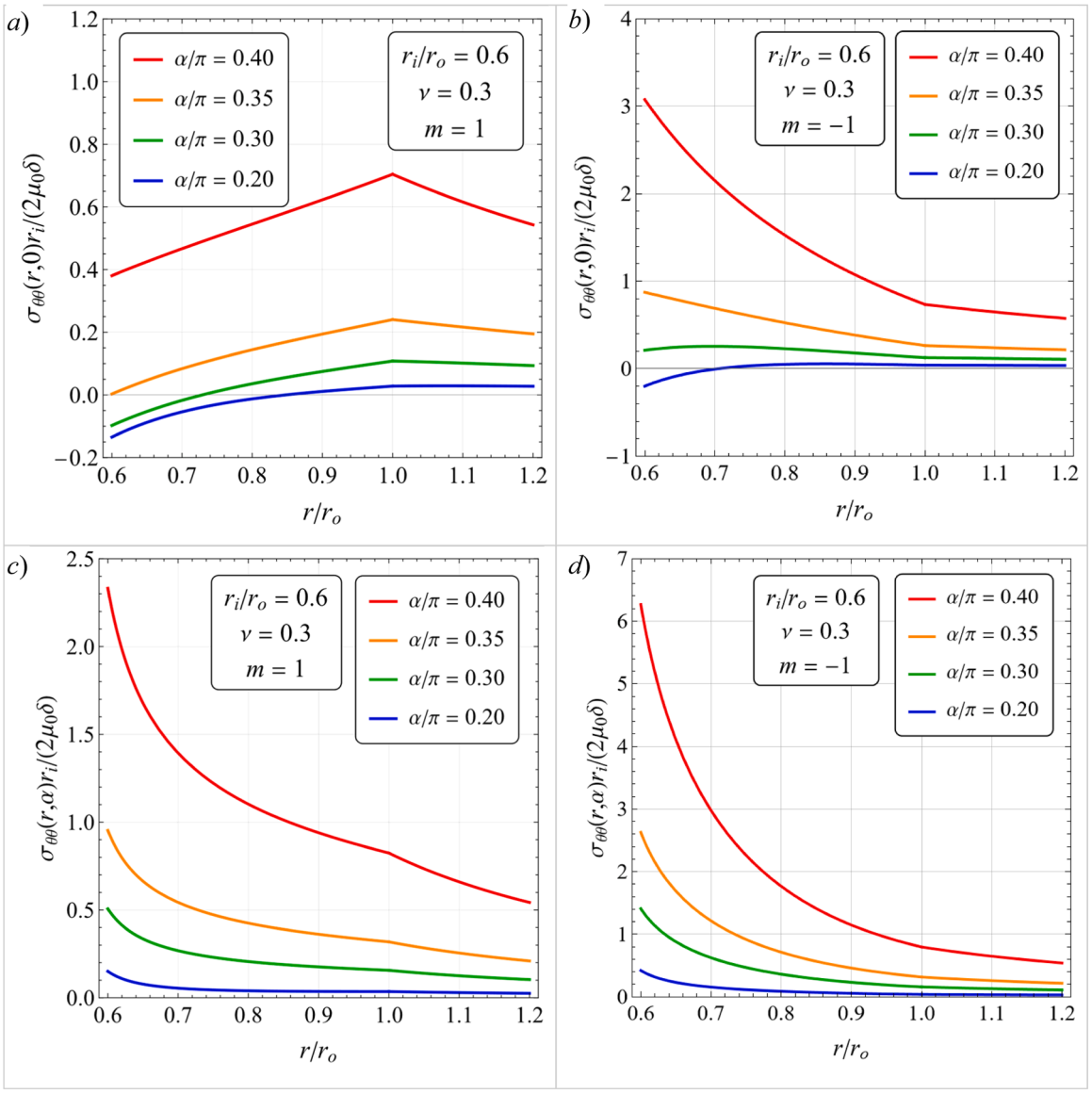

Fig. 10. Normalized variations of the hoop stress with the radial coordinate r along the radial directions $\theta = 0$ (*a, b*) and $\theta = \alpha$ (*c, d*), for various contact angles, for a positive grading index $m = 1$ (*a, c*) and a negative grading index $m = -1$ (*b, d*), for a FGM ring with aspect ratio $r_i/r_o = 0.6$.

$m = -1$ is about 2.7 times higher than for $m = 1$, under the same contact angular extent. When the contact angle and the pin load are small, the hoop stress can be negative (compressive) in a limited region near $\theta = 0$, where it reaches its minimum value. As the contact angle and the pin load increase, the hoop stress becomes positive (tensile) also at $\theta = 0$, whereas it becomes slightly negative at $\theta = \pi$.

The normalized variations of the contact pressure, $-\sigma_{rr}$, along the interface between a FGM ring with $r_i/r_o = 0.6$ and the infinite elastic plane, namely at $r = r_o$, are plotted in Figs. 9*a,b*, for various contact angles, both for $m = 1$ and $m = -1$. The magnitude of the contact pressure distribution displays a maximum at $\theta = 0$, it is compressive for small values of the angular coordinate θ slightly larger than the contact half-angle α, and it becomes tensile for larger values of θ. These results show that the contact pressure along the interface between the FGM ring and the elastic isotropic plate, under the same contact angle, for $m = -1$ (Fig. 9*b*) is a bit higher than that for $m = 1$ (Fig. 9*a*) of about 12 %. A similar result holds also for the normalized variations of the shear stress plotted in Figs. 9*c,d*. These variations display opposite signs for small and large values of the angular coordinate θ. The maximum shear stress occurs at an angular coordinate θ larger than $\pi/2$, and this maximum increases with the size of the contact half-angle α. In this case, however, the maximum shear stress for $m = -1$ is about 60 % higher than that for $m = 1$.

The normalized variations of the hoop stress with the angular coordinate θ along the interface between the FGM ring and the outer elastic plane, namely at $r = r_o$, are plotted in Fig. 9*e,f*, for various contact angles, for $m = 1$ and $m = -1$, respectively. The hoop stress is almost everywhere tensile on the outer surface of the FGM ring and it becomes compressive very near $\theta = \pi$, and its maximum is attained at about $\theta = 0.3\pi$. Moreover, the maximum hoop stress at $r = r_o$ for $m = 1$ and $m = -1$ is almost the same.

The normalized variations of the hoop stress along the radial directions $\theta = 0$ and $\theta = \alpha$, are plotted in Fig. 10, both for $m = 1$ and $m = -1$. These results clearly show that no jump in the hoop stress occurs at the interface between the FGM ring and the infinite elastic plane, because the elastic parameters are continuous across the interface. The trend of the hoop stress within the FGM ring at $\theta = 0$ displays a drastic change for positive and negative values of the grading index. Indeed, for positive m, the hoop stress in the FGM ring significantly decreases moving inwards from r_o to r_i (Fig. 10*a*) and it attains a maximum on the

outer surface of the FGM ring, whereas an opposite trend is observed for $m = -1$ (Fig. 10*b*). In this case, the maximum hoop stress shifts from the outer to the inner surface of the FGM ring, and its magnitude rapidly rises as the contact angle and pin load increase. This behavior aligns with earlier studies showing that in FGMs the stress distribution tends to follow the spatial gradient of the Young's modulus [23,79]. It can be shown that for $m \approx 0.25$, the hoop stress within the FGM ring is almost uniform along the radial line $\theta = 0$. As the grading index increases, the radial variation of the hoop stress decreases also at the angular coordinate $\theta = \alpha$, as shown in Figs. 10*c,d*. In particular, the maximum hoop stress along the radial line $\theta = \alpha$, which occurs at $r = r_i$, is reduced by about 63 % when m increases from -1 to 1. However, an almost uniform variation of the hoop stress along this radial direction occurs only for $m > 1$. This result is fully consistent with the findings in [52,53], which indicate that the optimal grading index for mitigating the SCF in a FGM ring inserted around a hole in a remotely loaded plate is approximately $m = 1.1$.

If the pin is inserted into a hole in a homogeneous material, it is reasonable to expect that reducing the contact pressure leads to an enhancement of the load-bearing capacity of the connection. However, if the material is inhomogeneous, the problem becomes considerably more complex. To evaluate the advantages produced by material grading, it becomes necessary to consider the effects of the variations of both the SCF and the material strength with the material grading. However, when designing with FGMs, it can be difficult to rely on a fixed allowable stress due to the lack of consistent data about FGM yield stress. Indeed, FGMs have a continuously changing material composition, which complicates the prediction of resulting material properties, with the exception of the Young's modulus. The latter can be accurately estimated by theoretical methods based on the Hashin-Shtrikman bounds in the absence of experimental data. It has been demonstrated that many porous materials, including cellular materials [80] and bones [81,82], generally exhibit power law variations in both strength and elastic modulus with density. In agreement with [13], it can thus be concluded that the most effective structural design can be achieved by maintaining radial variations in the effective stress and material strength to a nearly coinciding level.

An alternative approach to shape and material optimization is provided by the technique of topological optimization. In [83] the authors employed this technique on the basis of the minimization of the maximum von Mises equivalent stress, instead of trying to keep it under a fixed allowable stress. This technique has the potential to provide a valuable insight into the process of form finding, as well as facilitating the identification of optimal distributions of multi-materials to minimize stress concentration in contact problems.

In the following, the distribution of the von Mises equivalent stress is calculated, with the aim of ensuring that it remains below the allowable stress of the FGM. This approach allows us to take full advantage of the FGM's ability to reduce and/or migrate stress concentrations, which is the objective of the optimal material composition designing.

To explicitly display the effect of material grading on the effective stress reduction, in the following, the analytical distributions of the von Mises equivalent stress σ_{eq} in the FGM ring and in the isotropic elastic plane, under the pin load $P/(\mu_0\delta) = 20$, are plotted for different grading indices of the FGM ring. In particular, the analytical distribution of the normalized von Mises equivalent stress under plane strain loading condition, namely

$$\sigma_{eq} = \sqrt{(1-\nu+\nu^2)(\sigma_{rr}+\sigma_{\theta\theta})^2 - 3\,\sigma_{rr}\sigma_{\theta\theta} + 3\,\sigma_{r\theta}^2}, \tag{5.1}$$

are plotted in Fig. 11 for $r_i/r_o = 0.8$ and in Fig. 12 for $r_i/r_o = 0.6$, under the same pin load $P = 20\ \mu_0\delta$ for positive ($m = 1$), null ($m = 0$), and negative ($m = -1$) values of the grading index.

The maximum equivalent stress consistently occurs at the center of the inner rim of the FGM ring ($\theta = 0$). This maximum increases for negative grading indices and decreases for positive ones, in agreement

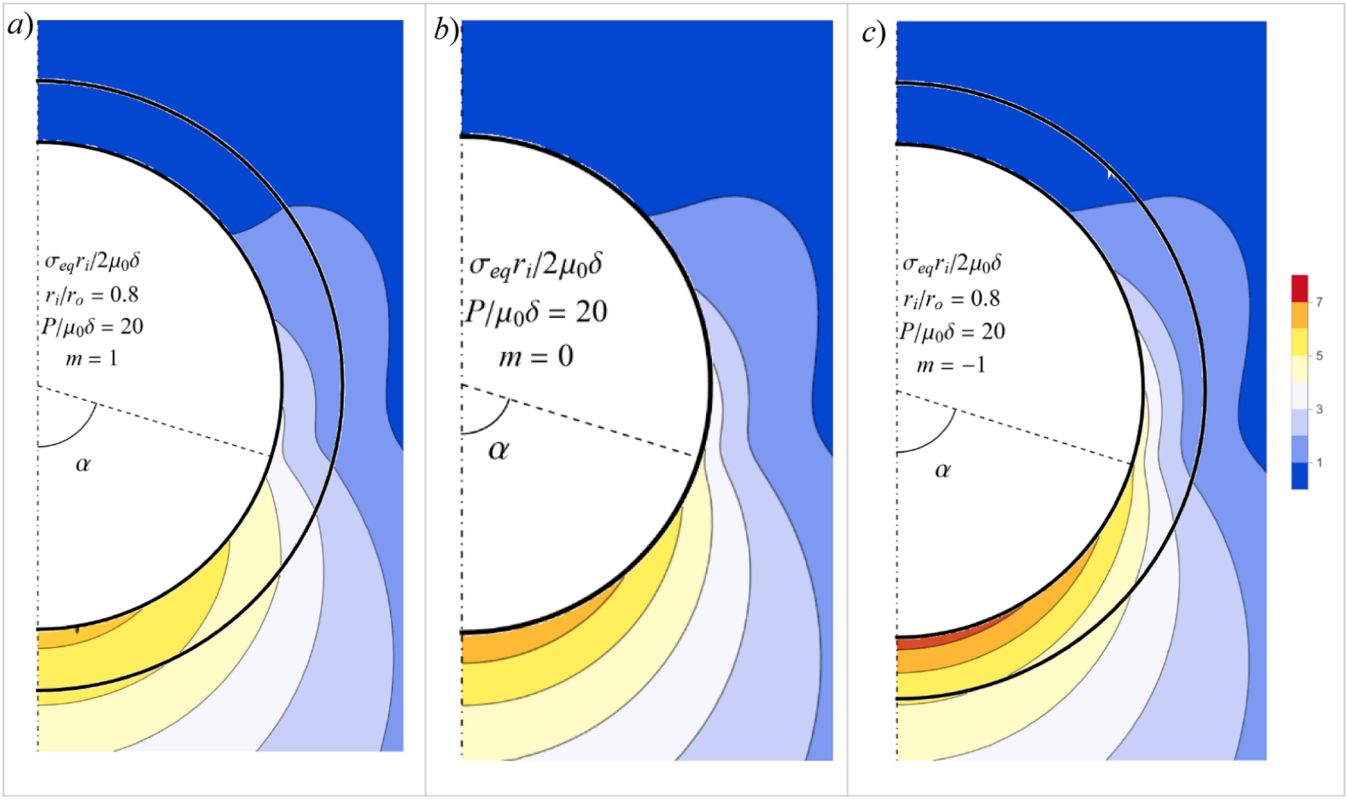

Fig. 11. Analytical distributions of the normalized von Mises equivalent stress $\sigma_{eq}r_i/(2\mu_0\delta)$ under plane strain condition in the FGM ring with aspect ratio $r_i/r_o = 0.8$ and the isotropic elastic plane, under the pin load $P/(\mu_0\delta) = 20$, for positive ($m = 1$) (*a*), null ($m = 0$) (*b*), and negative ($m = -1$) (*c*) grading indices.

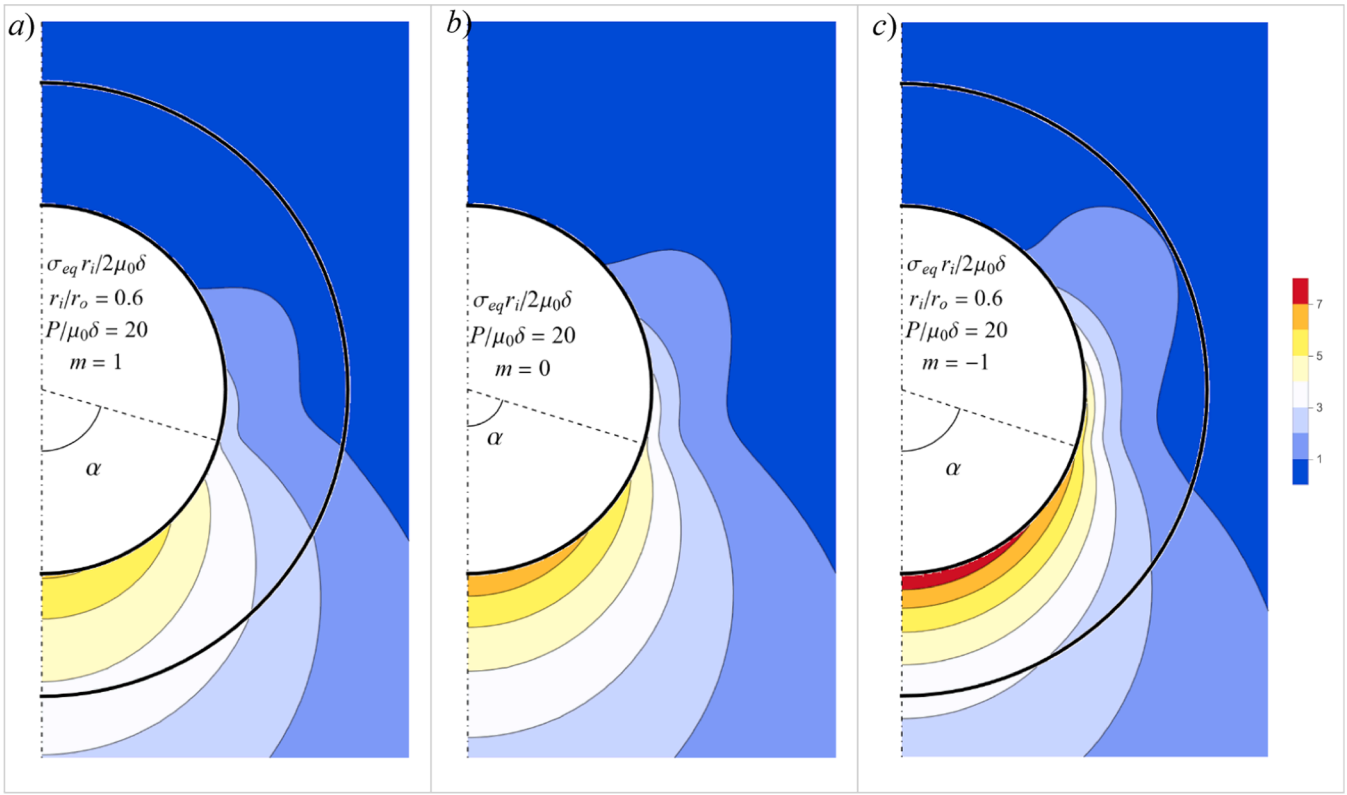

Fig. 12. Analytical distributions of the normalized von Mises equivalent stress $\sigma_{eq} r_i/(2\mu_0\delta)$ under plane strain condition in the FGM ring with aspect ratio $r_i/r_o = 0.6$ and the isotropic elastic plane, under the pin load $P/(\mu_0\delta) = 20$, for positive ($m = 1$) (*a*), null ($m = 0$) (*b*), and negative ($m = -1$) (*c*) grading indices.

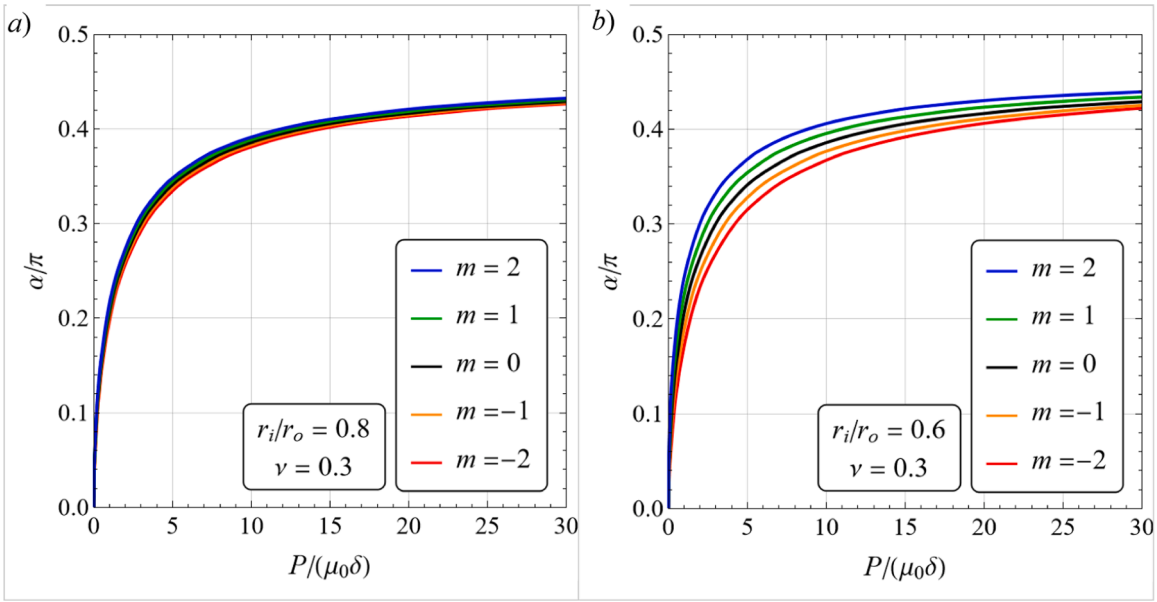

Fig. 13. Normalized variations of the contact half-angle α with the pin load *P* under plane stress condition for specific values of the grading index *m*, for a thin FGM ring with aspect ratio $r_i/r_o = 0.8$ (*a*), and a thicker FGM ring with $r_i/r_o = 0.6$ (*b*).

with the general trend that stress levels rise with increasing elastic modulus. Accordingly, FGMs with higher elastic moduli exhibit elevated stress concentrations, but also greater material strength, and vice versa. For instance, incorporating an FGM ring with a positive grading index (e.g., $m = 1$) can reduce the peak equivalent stress by approximately 14 % compared to the unreinforced case ($m = 0$), provided the ring is sufficiently thick (Fig. 12*a*). The reduction is slightly lower for thinner rings (Fig. 11*a*). This occurrence highlights the stress-shielding effect brought by a positively graded FGM ring, where the shear modulus decreases from the outer to the inner boundary (i.e., the shear modulus μ near the hole is lower than the shear modulus μ_0 of the outer elastic plane).

However, as a reduction in elastic modulus also entails reduced mechanical strength, a negatively graded FGM ($m < 0$) may be preferable if the material strength enhancement outweighs the associated equivalent stress increase. For example, with $m = -1$, the maximum

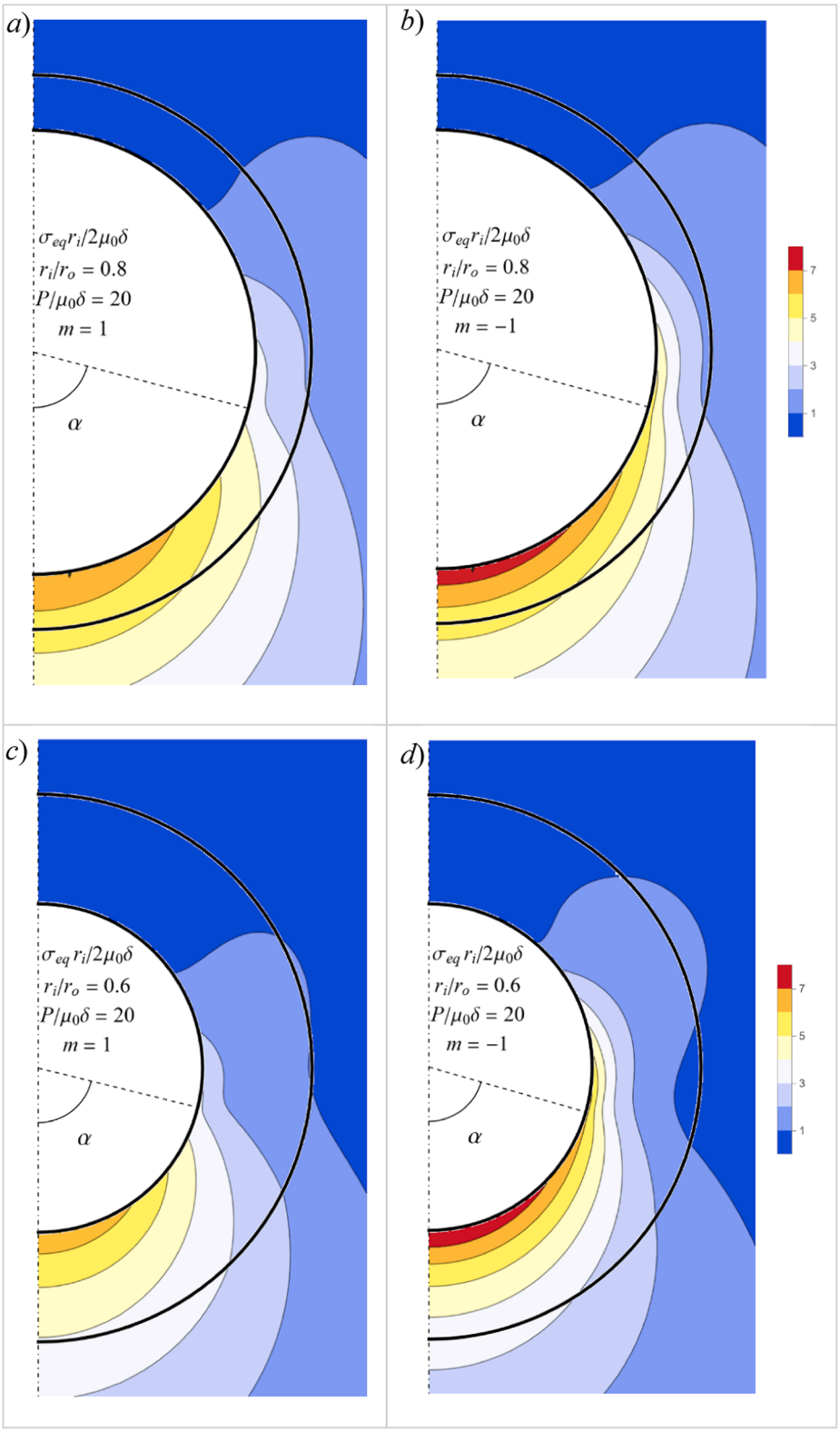

Fig. 14. Analytical distributions of the normalized von Mises equivalent stress $\sigma_{eq} r_i/(2\mu_0\,\delta)$ under plane stress condition in the FGM ring and in the isotropic elastic plane, under the same pin load $P/(\mu_0\delta) = 20$, for $m = 1$ and $r_i/r_o = 0.8$ (*a*), $m = -1$ and $r_i/r_o = 0.8$ (*b*), $m = 1$ and $r_i/r_o = 0.6$ (*c*), and $m = -1$ and $r_i/r_o = 0.6$ (*d*).

equivalent stress rises by about 10 % relative to the $m = 0$ case (Figs. 11*c* and 12*c*), but the corresponding increase in material strength may be more substantial.

These results are consistent with the known behavior of FGMs, where both stress and strength tend to follow the elastic modulus gradient: regions with higher stiffness bear greater loads and typically exhibit improved mechanical integrity due to reduced microdefect/porosity density. Thus, for $m < 0$, both stress and stiffness increase toward the inner rim, whereas the opposite trend is expected for $m > 0$. The results presented in Figs. 11 and 12 for $m = 1$ and $m = -1$ are validated in the Supplementary Material through comparison with FE simulations performed using Comsol 6.1. Additionally, the half contact angle α is

compared with the FE predictions, showing a maximum deviation of 5 %.

5.1. Results under plane stress loading condition

This subsection presents some results obtained under plane stress loading conditions, with the intention of bring out the small discrepancies observed when compared to the plane strain condition. In particular, the normalised variations of the contact half-angle α with the pin load P under plane stress loading conditions are plotted in Fig. 13 for the same geometrical and material parameters considered in Fig. 6. These outcomes show that the contact angle exhibits a slight increase under plane stress loading conditions in comparison with plane strain. Moreover, the contour plots of the normalized von Mises equivalent stress $\sigma_{eq}r_i/(2\mu_0\delta)$ under plane stress loading conditions, where

$$\sigma_{eq} = \sqrt{\sigma_{rr}^2 + \sigma_{\theta\theta}^2 - \sigma_{rr}\sigma_{\theta\theta} + 3\,\sigma_{r\theta}^2}, \tag{5.2}$$

are reported in Fig. 14 both in the FGM ring and isotropic elastic plane, in order to compare them with the corresponding plots obtained in Figs. 11 and 12 for the plane strain condition, under the same pin load $P = 20\mu_0\delta$, for $m = 1$ and $m = -1$. This comparison shows that the von Mises equivalent stress turns out to be a bit higher under plane stress loading condition, both in the FGM ring and in the outer elastic plane, specially for positive grading index ($m = 1$).

6. Validation of results by using the *M*-integral

In a homogeneous elastic material, the M-integral is an energy-based path-independent integral associated with scaling transformations (dilatation of the coordinate system), which is defined by:

$$M = \oint_C \left(w\,\mathbf{I} - \nabla\mathbf{u}^{\mathrm{T}}\boldsymbol{\sigma}\right)\mathbf{n}\cdot\mathbf{r}\,ds, \tag{6.1}$$

where $\boldsymbol{r} = r\,\mathbf{e}_r$ denotes the position vector in the plane, being $\mathbf{e}_r$ the unit vector along the radial direction, $w = w(\boldsymbol{\varepsilon})$ is the strain energy density, being $\boldsymbol{\varepsilon}$ the strain tensor, C is a counterclockwise contour enclosing a hole or inclusion, $\boldsymbol{n}$ denote the outward normal to the contour C. From the physical point of view, the M-integral calculated along a contour enclosing a hole represents the energy release due to an expansion of the hole [84].

In a radially inhomogeneous material the strain energy density depends on both the strain tensor $\boldsymbol{\varepsilon}$ and the radial distance r, namely $w = w(\boldsymbol{\varepsilon}, r)$. In this case, the M-integral is no longer path-independent and a correction term due to the material gradient must be added to the classical form (6.1). It can be proved that the following quantity must be invariant (Appendix B)

$$M(r) = \oint_{C(r)} \left(w\,\mathbf{I} - \nabla\mathbf{u}^{\mathrm{T}}\boldsymbol{\sigma}\right)\mathbf{n}\cdot\mathbf{r}\,ds + \int_r^{r_o} r^2 dr \int_{-\pi}^{\pi} \frac{\partial w}{\partial r}\,d\theta, \tag{6.2}$$

where $C(r)$ is the circle of radius $r < r_o$ surrounding the hole. Therefore, the contour term in (6.2) evaluated in the FGM ring depends on the radius r, but the combined expression $M(r)$ is invariant (in the absence of body forces and for solutions satisfying equilibrium and compatibility) provided that the area integral is included. Note that, for $r > r_o$, namely in the homogeneous elastic material $\partial w/\partial r = 0$, so that the area integral in (6.2) vanishes and the M-integral assumes the classical form (6.1). In practice, both terms in (6.2) must be considered to obtain a contour-independent value in a FGM. This is the key correction noted in the literature for FGM [85], viscoelastic [86], thermoelastic [87], and damaged/fractured solids [88].

One of the most practical and powerful uses of the M-integral (especially in FGMs) is to validate analytical or numerical results, because the M-integral provides a global, invariant energetic measure of the solution when all correction terms (such as the FGM gradient term) are properly included. Namely, if the M-integral is computed along several contours enclosing the hole and the same value is obtained, then the analytical stress and displacement fields satisfy equilibrium, compatibility, and constitutive relations consistently. Thus, the M-integral acts like an energy conservation check for the analytical fields. Therefore, we can use the invariant property of Eq. (6.2) to validate the analytical solution here obtained for a pin-loaded hole surrounded by a FGM ring embedded in an elastic homogeneous plane.

Under plane strain or plane stress loading conditions, the strain energy density for a radially inhomogeneous material with a constant Poisson ratio is defined as

$$w = w(\boldsymbol{\varepsilon}, r) = \mu(r)\left[\varepsilon_{rr}^2 + \varepsilon_{\theta\theta}^2 + 2\varepsilon_{r\theta}^2 + \frac{\bar{\nu}}{1-2\bar{\nu}}\,(\varepsilon_{rr} + \varepsilon_{\theta\theta})^2\right], \tag{6.3}$$

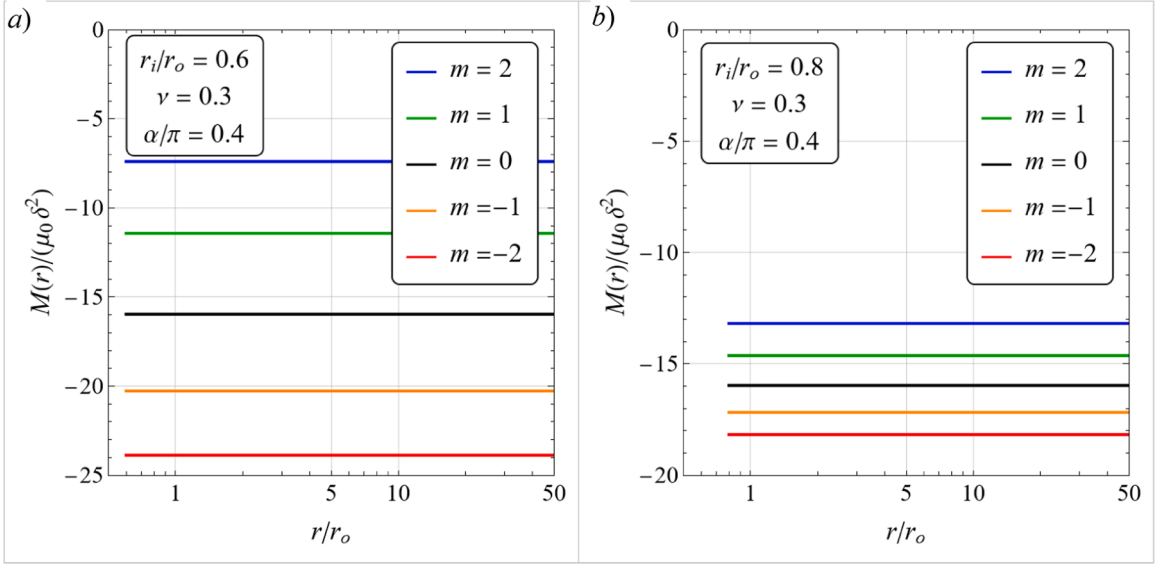

Fig. 15. Normalized variations of the M-integral with the radius r of the closed circular contour enclosing the pin-loaded hole for various values of the grading index m, and the aspect ratios $r_i/r_o = 0.6$ and $r_i/r_o = 0.8$, for the contact half-angle $\alpha/\pi = 0.4$.

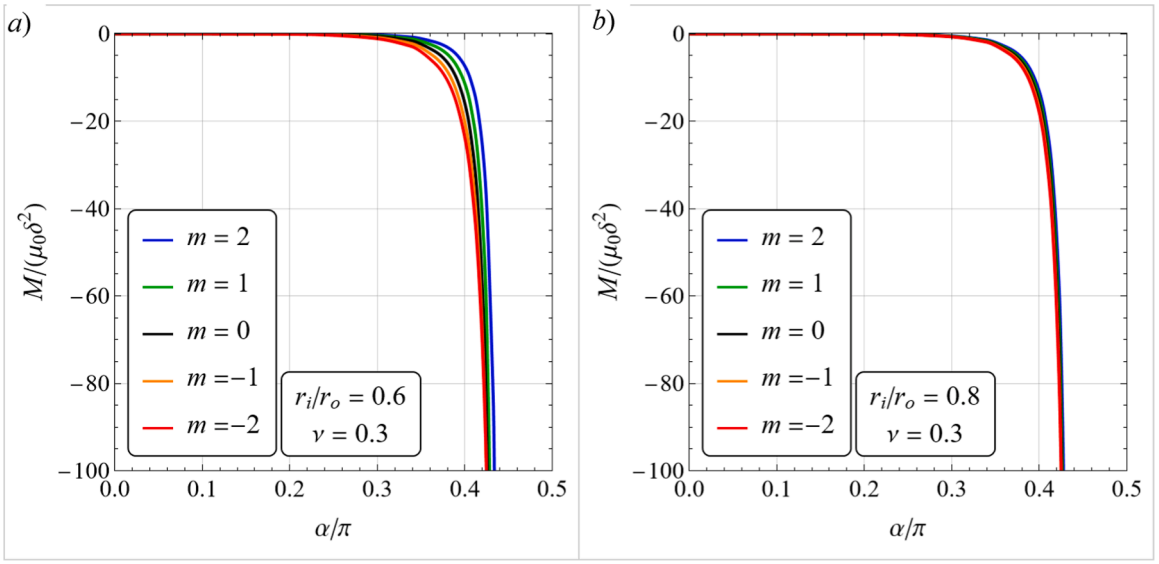

Fig. 16. Normalized variations of the M-integral with the contact half-angle α for various values of the grading index m and the aspect ratios $r_i/r_o = 0.6$ (a) and $r_i/r_o = 0.8$ (b).

where $\bar{\nu}$ has been defined in (2.4), then correspondingly

$$M(r) = \frac{r^2}{2}\int_{-\pi}^{\pi}\left[\sigma^0_{\theta\theta}\frac{u^0_{\theta,\theta}+u^0_r}{r} - \sigma^0_{rr}u^0_{r,r} - \sigma^0_{r\theta}\left(u^0_{\theta,r}+\frac{u^0_\theta - u^0_{r,\theta}}{r}\right)\right]d\theta, \tag{6.4}$$

for $r > r_o$, namely in the homogeneous elastic plane, and

$$\begin{aligned} M(r) \;=\; & \frac{r^2}{2}\int_{-\pi}^{\pi}\left[\sigma_{\theta\theta}\frac{u_{\theta,\theta}+u_r}{r} - \sigma_{rr}u_{r,r} - \sigma_{r\theta}\left(u_{\theta,r}+\frac{u_\theta - u_{r,\theta}}{r}\right)\right]d\theta \\ & + \frac{m}{4\mu_0}\int_r^{r_o} r^{1-m}dr\int_{-\pi}^{\pi}\left[(1-\bar{\nu})\left(\sigma^2_{rr}+\sigma^2_{\theta\theta}\right) - 2\bar{\nu}\sigma_{rr}\sigma_{\theta\theta} + 2\sigma^2_{r\theta}\right]d\theta, \end{aligned} \tag{6.5}$$

for $r_i \le r \le r_o$, namely in the FGM ring.

The variations of the M-integral, defined in Eqs. (6.4) and (6.5), with the radius r of the closed circular contour enclosing the pin-loaded hole under plane strain condition, are plotted in Figs. 15*a,b* for various values of the grading index m, and the aspect ratios $r_i/r_o = 0.6$ and $r_i/r_o = 0.8$, for $\alpha/\pi = 0.4$.

Here, the M-integral for the pin-loaded hole surrounded by a FGM ring is found to be constant for every values of r, thus validating the analytical results obtained for the stress and displacement fields both in the FGM ring and in the homogeneous elastic plane. Moreover, it turns out to be negative and its magnitude increases as the grading index decreases, as well as the contact angle increases, as illustrated in Fig. 16. The sign of the M-integral depends on the difference between the value of the strain energy term and the work of external forces. A negative M-integral around a loaded hole in an elastic material indicates that the total potential energy Π would increase under a virtual expansion of the hole, since $M = -\partial\Pi/\partial r_i$.

Although the M-integral is positive for a hole subjected to uniform internal pressure, a negative value can occur when the increase in strain energy outweighs the work performed by the boundary pressure. Specifically, the contact pressure on the hole rim does positive work during expansion, which tends to reduce Π, while the surrounding material stores additional strain energy. When the net effect of strain energy increase dominates, the M-integral becomes negative, reflecting a configuration that resists expansion. Fig. 15 shows that an increase in the shear modulus of the FGM ring, which corresponds to larger negative values of the grading index, yields a corresponding increase in the magnitude of the negative M-integral. Moreover, as the contact half-angle α tends to its limit value, a bit lower than π/2, the magnitude of the M-integral becomes unbounded.

7. Conclusions

An analytical solution has been obtained for the contact problem involving a loaded, rigid, circular pin in contact with an infinite elastic plate containing a hole of a slightly larger radius surrounded by a FGM ring with power-law radial grading of the elastic shear modulus. The same constant Poisson ratio has been considered both for the FGM ring and the elastic plane. Assuming a Michell-type series representation for the stress and displacement fields, the mixed boundary value problem has been first transformed into a dual trigonometric series problem, which is then reduced to a linear system of infinite equations and finally solved by truncation. Both conditions of plane strain and plane stress have been considered here. The focus is on the possibility of reducing the peaks in the contact pressure and hoop stress by adopting an optimal radial variation of the shear modulus of the FGM ring.

Results such as pin load-contact angle relations, contact pressure distributions, and stress distributions within the FGM ring and the elastic plane are obtained in closed form for various grading parameters, aspect ratios, and loading levels, then validated against FE simulations and using the invariance properties of the M-integral. From these results, the progressive contact between the pin and the inner surface of the FGM ring can be clearly observed in the presence of clearance. In particular, the size of the contact region is found to increase non-linearly with the pin load and to approach an asymptotic value lower than π/2 as the pin load increases. The contact pressure exhibits an almost Hertzian distribution for all load levels and contact zone sizes, thus it vanishes at the contact ends and attains a maximum at the centre of the contact region.

The introduction of a FGM ring with a positive grading index allows to reduce the hoop stress and von Mises equivalent stress. Indeed, if the shear modulus of the FGM ring progressively decreases towards the inner ring surface then the FGM in contact with the rigid pin is more compliant and thus the size of the contact region becomes larger. Consequently, a reduction of the contact pressure is observed. However, for positive grading index also the FGM strength decreases with the elastic modulus near the inner rim of the ring. For negative grading index instead, the stress level increases at the inner rim ring, just where the material is stronger, whereas it decreases within the ring thickness

and in the elastic plane. If the increase in the material strength is more substantial than the increase in the stress level, then a FGM ring with negative grading indices can shield the elastic plane by localizing stress in the stiffer inner region, which is also the strongest.

Graphical results and comparisons with the solution of the problem without the FGM ring, namely for $m = 0$, can help mechanical and material scientists to design new tailored materials that can increase the load-bearing capacity of pinned connections by exploiting the peculiar properties of FGMs.

The present analytical solutions could also be useful for validating further theoretical and numerical investigations on FGM pin-loaded joints. A further generalization of the present approach may include the elastic deformability of the pin, which can be easily implemented within the current approach. Most importantly, experimental results are needed to validate the load-bearing capacity of the pin in hole connection according to the variation of the strength with the elastic modulus, which depend on the specific kind of FGM.

In conclusion, we have demonstrated that is possible to reduce the stress concentration factor created by the load transmitted by a stiff circular pin to the rim of a hole in an elastic isotropic plane by inserting an FGM ring around the hole, whose thickness and variation of the elastic properties along the thickness are chosen appropriately. The findings of the present study offer valuable insights for the effective design of a number of structural pinned connections, including bearing bolt connections and aircraft skin fasteners, by exploiting the innovative capabilities provided by FGMs.

Author statement

The author confirms that this manuscript is original and has not been published previously, nor is it under consideration for publication elsewhere. The author declares that there are no conflicts of interest related to this work.

CRediT authorship contribution statement

E. Radi: Writing – review & editing, Writing – original draft, Visualization, Validation, Supervision, Software, Methodology, Investigation, Formal analysis.

Declaration of competing interest

The authors declare that they have no known competing financial interests or personal relationships that could have appeared to influence the work reported in this paper.

Acknowledgments

Support by the National Group of Mathematical Physics (GNFM-INdAM) is gratefully acknowledged.

Supplementary materials

Supplementary material associated with this article can be found, in the online version, at doi:10.1016/j.ijmecsci.2025.111048.

Appendix A

The set of dual Eqs. (2.16)$_1$ and (2.21) can be solved for the coefficients A_n, ($n = 0, 1, 2,\ldots$) by using the procedure proposed in [73,89] and adopted also in [66–68], based on the introduction of an auxiliary stress function φ such that

$$\frac{A_0}{2}+\sum_{n=1}^{\infty}A_n\cos n\theta = H(\alpha-\theta)\cos\frac{\theta}{2}\int_{\theta}^{\alpha}\frac{\varphi(s)\,\mathrm{d}s}{\sqrt{\cos\theta-\cos s}}, \quad \text{for } 0\le|\theta|\le\pi. \tag{A.1}$$

where $H(\alpha-t)$ is the Heaviside unit step function. Then, the coefficients A_n, for $n = 0, 1, 2,\ldots$, of the Fourier cosine series expansion (A.1) are given in [67,73,89]:

$$A_0 = \frac{2}{\pi}\int_0^{\alpha}\cos\frac{\theta}{2}\mathrm{d}\theta\int_{\theta}^{\alpha}\frac{\varphi(s)\,\mathrm{d}s}{\sqrt{\cos\theta-\cos s}} = \frac{2}{\pi}\int_0^{\alpha}\varphi(s)\mathrm{d}s\int_0^{s}\frac{\cos(\theta/2)\,\mathrm{d}\theta}{\sqrt{\cos\theta-\cos s}} = \sqrt{2}\int_0^{\alpha}\varphi(s)\mathrm{d}s, \tag{A.2}$$

$$\begin{aligned} A_n &= \frac{2}{\pi}\int_0^{\alpha}\cos\frac{\theta}{2}\cos n\theta\,\mathrm{d}\theta\int_{\theta}^{\alpha}\frac{\varphi(s)\,\mathrm{d}s}{\sqrt{\cos\theta-\cos s}} = \frac{2}{\pi}\int_0^{\alpha}\varphi(s)\mathrm{d}s\int_0^{s}\frac{\cos(\theta/2)\cos n\theta}{\sqrt{\cos\theta-\cos s}}\mathrm{d}\theta \\ &= \frac{1}{\pi}\int_0^{\alpha}\varphi(s)\mathrm{d}s\int_0^{s}\frac{\cos(n+1/2)\theta+\cos(n-1/2)\theta}{\sqrt{\cos\theta-\cos s}}\mathrm{d}\theta = \frac{1}{\sqrt{2}}\int_0^{\alpha}[P_n(\cos s)+P_{n-1}(\cos s)]\varphi(s)\mathrm{d}s,\ (n=1,2,\ldots), \end{aligned} \tag{A.3}$$

where the following Mehler's integral for the Legendre polynomial ([73], Eq. 2.6.20) has been used

$$\int_0^{s}\frac{\cos(n+1/2)\theta}{\sqrt{\cos\theta-\cos s}}\,\mathrm{d}\theta = \frac{\pi}{\sqrt{2}}P_n(\cos s),\ (n=0,1,2,\ldots). \tag{A.4}$$

Now, using Eq. (A.3) and the following result ([73], eqn 2.6.31)

$$\frac{1}{\sqrt{2}}\sum_{n=1}^{\infty}[P_n(\cos s)+P_{n-1}(\cos s)]\sin n\theta = \frac{H(\theta-s)\cos(\theta/2)}{\sqrt{\cos s-\cos\theta}}, \tag{A.5}$$

from Eq. (2.21) it follows

$$\int_0^{\theta}\frac{\varphi(s)\,\mathrm{d}s}{\sqrt{\cos s-\cos\theta}} = \frac{1}{\cos(\theta/2)}\left[(cA_0+d)\theta+\sum_{n=1}^{\infty}h_nA_n\sin n\theta\right], \quad \text{for } 0\le|\theta|\le\alpha, \tag{A.6}$$

which is an integral equation of the Abel type. Then, Eq. (A.6) can be inverted to obtain the auxiliary stress function φ, namely

$$\varphi(s)=\frac{2}{\pi}\frac{\mathrm{d}}{\mathrm{d}s}\int_0^s\frac{\sin(\theta/2)}{\sqrt{\cos\theta-\cos s}}\left[(cA_0+d)\theta+\sum_{n=1}^{\infty}h_nA_n\sin n\theta\right]\mathrm{d}\theta, \tag{A.7}$$

Using the following integral provided in the appendix of [38]

$$\int_0^s\frac{\theta\sin(\theta/2)}{\sqrt{\cos\theta-\cos s}}\mathrm{d}\theta=-\sqrt{2}\pi\ln\left(\cos\frac{s}{2}\right), \tag{A.8}$$

and the result

$$\int_0^s\frac{\sin(\theta/2)\,\sin n\theta}{\sqrt{\cos\theta-\cos s}}\mathrm{d}\theta=\frac{\pi}{2\sqrt{2}}[P_{n-1}(\cos s)-P_n(\cos s)],\quad(n=1,2,\ldots), \tag{A.9}$$

which follows from Eq. (A.4), the integrals in eqn (A.7) can be calculated in closed form, thus obtaining

$$\varphi(s)=\frac{1}{\sqrt{2}}\frac{\mathrm{d}}{\mathrm{d}s}\left\{-4(cA_0+d)\ln\left(\cos\frac{s}{2}\right)+\sum_{n=1}^{\infty}h_nA_n[P_{n-1}(\cos s)-P_n(\cos s)]\right\}, \tag{A.10}$$

namely

$$\varphi(s)=\frac{1}{\sqrt{2}}\left\{2(cA_0+d)+\sum_{n=1}^{\infty}nh_nA_n[P_n(\cos s)+P_{n-1}(\cos s)]\right\}\tan\frac{s}{2}. \tag{A.11}$$

Then, using the results

$$\int_0^{\alpha}[P_n(\cos s)+P_{n-1}(\cos s)]\tan\frac{s}{2}\mathrm{d}s=\frac{1}{n}[P_{n-1}(\cos\alpha)-P_n(\cos\alpha)], \tag{A.12}$$

$$\int_0^{\alpha}[P_n(\cos s)+P_{n-1}(\cos s)]\left[P_j(\cos s)+P_{j-1}(\cos s)\right]\tan\frac{s}{2}\mathrm{d}s=\frac{(1+\cos\alpha)\sin^2\alpha}{2\left(n^2-j^2\right)}\left[(n+1)P_{j-1}^{(0,1)}(\cos\alpha)P_{n-2}^{(1,2)}(\cos\alpha)-(j+1)P_{n-1}^{(0,1)}(\cos\alpha)P_{j-2}^{(1,2)}(\cos\alpha)\right], \tag{A.13}$$

provided in the appendix in [68], the introduction of eqn (A.11) in (A.2) and (A.3) yields the relations (2.24) and (2.25) for the coefficients A_n, for $n=0, 1, 2,\ldots$

Appendix B

Path dependence of the contour M-integral for FGMs follows from the transformation into an area integral evaluated on the area A surrounded by the closed contour C, whose outward normal unit vector is denoted by $\boldsymbol{n}$. Indeed, it is easy to prove that

$$\mathrm{div}(w\mathbf{r}-\boldsymbol{\sigma}\nabla\mathbf{u}\,\mathbf{r})=2w+\mathbf{r}\cdot\nabla w-\boldsymbol{\sigma}\cdot[\nabla\mathbf{u}+(\nabla\nabla\mathbf{u})\mathbf{r}]-(\nabla\mathbf{u})\,\mathbf{r}\cdot\mathrm{div}\,\boldsymbol{\sigma}. \tag{B1}$$

Then, by using the balance condition in the absence of body forces, $\mathrm{div}\,\boldsymbol{\sigma}=\mathbf{0}$, the compatibility condition $\boldsymbol{\varepsilon}=(\nabla\mathbf{u}+\nabla\mathbf{u}^{\mathrm{T}})/2$, and the definition of strain energy density, $2w=\boldsymbol{\sigma}:\boldsymbol{\varepsilon}$, one obtains

$$\mathrm{div}(w\mathbf{r}-\boldsymbol{\sigma}\nabla\mathbf{u}\,\mathbf{r})=\mathbf{r}\cdot(\nabla w-\boldsymbol{\sigma}\cdot\nabla\nabla\mathbf{u})=\mathbf{r}\cdot\left(\nabla w-\frac{\partial w}{\partial\boldsymbol{\varepsilon}}\cdot\nabla\boldsymbol{\varepsilon}\right)=\mathbf{r}\cdot\frac{\partial w}{\partial r}\nabla r=\frac{\partial w}{\partial r}r. \tag{B2}$$

Using relations (A2) and the Gauss-Green theorem, it straight follows that

$$\oint_C(w\mathbf{I}-\nabla\mathbf{u}^{\mathrm{T}}\boldsymbol{\sigma})\mathbf{n}\cdot\mathbf{r}\,\mathrm{d}s=\int_A\mathrm{div}(w\,\mathbf{r}-\boldsymbol{\sigma}\nabla\mathbf{u}\,\mathbf{r})\mathrm{d}A=\int_A\frac{\partial w}{\partial r}r\;\mathrm{d}A, \tag{B3}$$

where C is an arbitrary closed contour surrounding the area A. The result (6.2) is then obtained by considering the annular region A between the outer circle of arbitrary radius $r>r_i$ and the inner circle of radius r_i coincident with the hole rim. For a homogeneous elastic material the strain density does not depend explicitly on r, and thus Eq. (B.3) implies path-independence of the M-integral.

Data availability

No data was used for the research described in the article.

References

[1] Mencik J. Mechanics of components with treated or coated surfaces, 42. Springer Science & Business Media; 2013.
[2] Osborn HB. Surface hardening by induction. Trans Electrochem Soc 1941;79(1):215.
[3] Persson E, Eriksson I, Hammersberg P. Propagation of hole machining defects in pin-loaded composite laminates. J Compos Mater 1997;31(4):383–408.
[4] Chau KT, Wei XX. Stress concentration reduction at a reinforced hole loaded by a bonded circular inclusion. J Appl Mech 2001;68(3):405–11.
[5] Akbarpour S, Hallström S. Reinforcement around holes in composite materials by use of patched metal inserts. Compos Struct 2019;225:111084.
[6] To QD, He QC, Cossavella M, Morcant K, Panait A. Closed-form solution for the contact problem of reinforced pin-loaded joints used in glass structures. Int J Solids Struct 2007;44(11–12):3887–903.
[7] To QD, He QC, Cossavella M, Morcant K, Panait A, Yvonnet J. Failure analysis of tempered glass structures with pin-loaded joints. Eng Fail Anal 2007;14(5):841–50.
[8] Zhang C, Chen F, Huang Z, Jia M, Chen G, Ye Y, Lin Y, Liu W, Chen B, Shen Q, Zhang L, Lavernia EJ. Additive manufacturing of functionally graded materials: a review. Mater Sci Eng A 2019;764:138209.
[9] Kumar P, Sharma SK, Singh RKR. Recent trends and future outlooks in manufacturing methods and applications of FGM: a comprehensive review. Mater Manuf Process 2023;38(9):1033–67.
[10] Zhang B, Jaiswal P, Rai R, Nelaturi S. Additive manufacturing of functionally graded material objects: a review. J Comput Inf Sci Eng 2018;18(4):041002.
[11] Giannakopoulos AE, Suresh S. Indentation of solids with gradients in elastic properties: part I. Point force. Int J Solids Struct 1997;34(19):2357–92.
[12] Giannakopoulos AE, Suresh S. Indentation of solids with gradients in elastic properties: part II. Axisymmetric indentors. Int J Solids Struct 1997;34(19):2393–428.
[13] Ciavarella M. Cancelling the effect of sharp notches or cracks with graded elastic modulus materials. J Mech Phys Solids 2024;192:105809.
[14] Çömez İ. Contact problem for a functionally graded layer indented by a moving punch. Int J Mech Sci 2015;100:339–44.
[15] Suresh S. Graded materials for resistance to contact deformation and damage. Sci 2001;292:2447–51.
[16] Suresh S, Olsson M, Giannakopoulos AE, Padture NP, Jitcharoen J. Engineering the resistance to sliding-contact damage through controlled gradients in elastic properties at contact surfaces. Acta Mater 1999;47(14):3915–26.
[17] Alkunte S, Fidan I, Naikwadi V, Gudavasov S, Ali MA, Mahmudov M, Hasanov S, Cheepu M. Advancements and challenges in additively manufactured functionally graded materials: a comprehensive review. J Manuf Mater Proc 2024;8(1):23.
[18] Mohammadi M, Dryden JR. Thermal stress in a nonhomogeneous curved beam. J Therm Stress 2008;31(7):587–98.
[19] Ebhota WS, Karun AS, Inambao FL. Centrifugal casting technique baseline knowledge, applications, and processing parameters: overview. Int J Mater Res 2016;107(10):960–9.
[20] Pradeep AD, Rameshkumar T. Review on centrifugal casting of functionally graded materials. Mater Today: Proc 2021;45:729–34.
[21] Bi G, Sun CN, Gasser A. Study on influential factors for process monitoring and control in laser aided additive manufacturing. J Mater Process Technol 2013;213(3):463–8.
[22] Tutuncu N. Stresses in thick-walled FGM cylinders with exponentially-varying properties. Eng Struct 2007;29(9):2032–5.
[23] Abdalla HMA, Casagrande D, De Bona F. Analysis of stress concentration in functionally graded plates with linearly increasing Young's modulus. Mater 2023;16(21):6882.
[24] Arslan E, Haskul M. Generalized plane strain solution of a thick-walled cylindrical panel subjected to radial heating. Acta Mech 2015;226:1213–25.
[25] Eroglu U. Large deflection analysis of planar curved beams made of functionally graded materials using variational iterational method. Compos Struct 2016;136:204–16.
[26] Pei YL, Li LX. A simplified theory of FG curved beams. Eur J Mech A/Solids 2021;85:104126.
[27] Li H, Liu Y. Functionally graded hollow cylinders with arbitrary varying material properties under nonaxisymmetric loads. Mech Res Comm 2014;55:1–9.
[28] Arasan U, Venkatachalam S, Murthy H. Solution to two-dimensional elastic problems involving functionally graded material in radial co-ordinates. Acta Mech 2022;233(1):343–62.
[29] Batra RC, Nie GJ. Analytical solutions for functionally graded incompressible eccentric and non-axisymmetrically loaded circular cylinders. Compos Struct 2010;92(5):1229–45.
[30] Nie GJ, Batra RC. Exact solutions and material tailoring for functionally graded hollow circular cylinders. J Elast 2010;99:179–201.
[31] Vasu TS, Bhandakkar TK. Plane strain cylindrical indentation of functionally graded half-plane with exponentially varying shear modulus in the presence of residual surface tension. Int J Mech Sci 2018;135:158–67.
[32] Guleid H, Faal RT, Fotuhi AR, Milani AS. A generalization and application of the Michell solution for functionally graded circular planes. Z Angew Math Phys 2022;73:1–31.
[33] Chawde DP, Bhandakkar TK. Mixed boundary value problems in power-law functionally graded circular annulus. Int J Press Vessel Pip 2021;192:104402.
[34] Liu CS, Zhang K, Yang R. The FEM analysis and approximate model for cylindrical joints with clearances. Mech Mach Theory 2007;42(2):183–97.
[35] Duc ND. Pin-loaded hole contact in an anisotropic magnetoelectroelastic plate. Int J Mech Sci 2025:110551.
[36] Li Y, Huang R, Zhao S, Wang J. Contact pressure analysis of pin-loaded lug with clearance. Adv Mech Eng 2022;14(6):16878132221107475.
[37] Persson A. PhD. Dissertation. Sweden: Chalmers University; 1964.
[38] Noble B, Hussain MA. Exact solution of certain dual series for indentation and inclusion problems. Int J Eng Sci 1969;7(11):1149–61.
[39] Rao AK, Eshwar VA, Dattaguru B. A comprehensive study of interference and clearance fit pins in large planes. Mech Res Commun 1977;4(5):325–32.
[40] Rao AK. Elastic analysis of pin joints. Compos Struct 1978;9:125–44.
[41] Ho KC, Chau KT. An infinite plane loaded by a rivet of a different material. Int J Solids Struct 1997;34(19):2477–96.
[42] Ciavarella M, Decuzzi P. The state of stress induced by the plane frictionless cylindrical contact. I. The case of elastic similarity. Int J Solids Struct 2001;38(26–27):4507–23.
[43] Ciavarella M, Decuzzi P. The state of stress induced by the plane frictionless cylindrical contact. II. The general case (elastic dissimilarity). Int J Solids Struct 2001;38(26–27):4525–33.
[44] Hou JP, Hills DA. Contact between a pin and a plane with a hole under interference-fit and clearance-fit conditions. Proc Inst Mech Eng C: J Mech Eng Sci 2001;215(6):629–39.
[45] Iyer K. Solutions for contact in pinned connections. Int J Solids Struct 2001;38(50–51):9133–48.
[46] Sundaram N, Farris TN. Mechanics of advancing pin-loaded contacts with friction. J Mech Phys Solids 2010;58(11):1819–33.
[47] Sundaram N, Farris TN. The generalized advancing conformal contact problem with friction, pin loads and remote loading-case of rigid pin. Int J Solids Struct 2010;47(6):801–15.
[48] de Jong T. Stresses around pin-loaded holes in elastically orthotropic or isotropic plates. J Compos Mater 1977;11(3):313–31.
[49] Mizushima I, Hamada M. Stress analysis around circular hole in infinite plate with rigid disk. Bull JSME 1983;26(218):1296–301.
[50] Nguyen VL, Nguyen VT, Duc ND. Pin-loaded hole contact in an anisotropic magnetoelectro-elastic plate. Int J Mech Sci 2025;302:110551.
[51] Kubair DV, Bhanu-Chandar B. Stress concentration factor due to a circular hole in functionally graded panels under uniaxial tension. Int J Mech Sci 2008;50(4):732–42.
[52] Mohammadi M, Dryden JR, Jiang L. Stress concentration around a hole in a radially inhomogeneous plane. Int J Solids Struct 2011;48:483–91.
[53] Sburlati R. Stress concentration factor due to a functionally graded ring around a hole in an isotropic plane. Int J Solids Struct 2013;50(22–23):3649–58.
[54] Sburlati R, Atashipour SR, Atashipour SA. Reduction of the stress concentration factor in a homogeneous panel with hole by using a functionally graded layer. Compos B: Eng 2014;61:99–109.
[55] Nie GJ, Zhong Z, Batra RC. Material tailoring for reducing stress concentration factor at a circular hole in a functionally graded material (FGM) panel. Compos Struct 2018;205:49–57.
[56] Nie GJ, Batra RC. Reducing stress concentration factor by strengthening circular hole with functionally graded incompressible material layer. Thin-Walled Struct 2019;144:106223.
[57] Andreev VI, Cybin NY. The inhomogeneous plate with a hole: kirsch's problem. Procedia Eng 2014;91:26–31.
[58] Goyat V, Verma S, Garg RK. Stress concentration reduction using different functionally graded materials layer around the hole in an infinite panel. Strength Fract Complex 2019;12(1):31–45.
[59] Hart EL, Terokhin BI. Finite-element analysis of stress concentration in thin plates and cylindrical shells with a circular hole surrounded by an inclusion of functionally graded material. J Math Sci 2025;291(5):1–13.
[60] Hart EL, Terokhin BI. Effect of functionally graded inclusion on stress conservation near a circular hole in thin plates for different boundary conditions. J Optim Differ Equ Appl 2025;33(1):110–27.
[61] Abdalla HMA, De Bona F, Casagrande D. Optimization of functionally graded materials to make stress concentration vanish in a plate with circular hole. Compos C: Open Access 2024;15:100512.
[62] Zhou Y, Lin Q, Hong J, Yang N. Optimal design of functionally graded material for stress concentration reduction. Struct 2021;29:561–9.
[63] Ke LL, Wang YS. Two-dimensional contact mechanics of functionally graded materials with arbitrary spatial variations of material properties. Int J Solids Struct 2006;43(18–19):5779–98.
[64] Alinia Y, Asiaee A, Hosseini-nasab M. Stress analysis in rolling contact problem of a finite thickness FGM layer. Meccanica 2019;54(1):183–203.
[65] Bahri A, Akhlaghi M, Salehi M. An exact solution for improved metal-composite joints reinforced by FG inter-layers. Sci Eng Compos Mater 2017;24(2):221–35.
[66] Radi E, Falope FO, Lanzoni L. Advancing contact between a rigid pin and a FGM circular beam with clearance. Int J Solids Struct 2025;311:113244.
[67] Block JM, Keer LM. Partial contact of an elastic coated cylinder pressed by a rigid flat surface. J Tribol 2007;129(1):60–4.
[68] Radi E, Strozzi A. Advancing contact of a 2D elastic curved beam indented by a rigid pin with clearance. Int J Nonlin Mech 2023;149:104313.
[69] Barber JR. Elasticity. 3rd revised editor. New York: Springer International Publishing; 2010.
[70] Singh G, Bhandakkar TK. Simplified approach to solution of mixed boundary value problems on homogeneous circular domain in elasticity. ASME J Appl Mech 2019;86(2):021007.
[71] Omar T, Hassan HA. Approximate solution for an indentation problem using dual series equations. Int J Eng Sci 1991;29(2):187–94.
[72] Hassan HAZ. Concentrated force acting on an elastic inclusion in a thick-walled tube. J Eng Math 1997;32:73–86.

[73] Sneddon IN. Mixed boundary value problems in potential theory. New York: John Wiley; 1966.
[74] Radi E. Dual series solution for the standardized ISRM Brazilian disc test modelled as an advancing contact problem. Int J Rock Mech Min Sci 2024;173:105634.
[75] Noble B, Whiteman JR. Solution of dual trigonometric series using orthogonality relations. SIAM J Appl Math 1970;18(2):372–9.
[76] Derevyagin M, Juricic N. An asymptotic formula for integrals of products of jacobi polynomials. J Stoch Anal 2020;1(4):8.
[77] Lanczos C. Applied analysis. Englewood Cliffs: Prentice Hall; 1956.
[78] Guler MA, Erdogan F. Contact mechanics of two deformable elastic solids with graded coatings. Mech Mater 2006;38(7):633–47.
[79] Fukui Y, Yamanaka N. Elastic analysis for thick-walled tubes of functionally graded material subjected to internal pressure. JSME Int J 1 1992;35(4):379–85.
[80] Gibson LJ. Modelling the mechanical behavior of cellular materials. Mater Sci Eng A 1989;110:1–36.
[81] Currey JD. The effect of porosity and mineral content on the Young's modulus of elasticity of compact bone. J Biomech 1988;21(2):131–9.
[82] Martin RB. Determinants of the mechanical properties of bones. J Biomech 1991; 24:79–88.
[83] Silva RF, Coelho PG, Conde FM, Santos BR, Oliveira JP. Minimizing the maximum von Mises stress of elastic continuum structures using topology optimization and additively manufactured functionally graded materials. Comput Struct 2024;301: 107469.
[84] Yi-Feng H, Chen YH. The area contraction and expansion for a nano-void under four different kinds of loading. Arch ApplMech 2011;81(9):1323–31.
[85] Hui T, Chen YH. The M-integral analysis for a nano-inclusion in plane elastic materials under uni-axial or bi-axial loadings. J Appl Mech 2010;77:1–9. 21019.
[86] Hou J, Zhang C, Li Q. The concept and numerical evaluation of M-integral based on domain integral method in cracked viscoelastic materials. Mech Mater 2020;145: 103363.
[87] Radi E, Morini L, Sevostianov I. Conservation integrals for two circular holes kept at different temperatures in a thermoelastic solid. Int J Solids Struct 2016;85:1–14.
[88] Hou J, Lv J, Ricoeur A, Hu Y, Zuo H, Chen Y, Li Q. The M-integral in fracture and damage mechanics: a review of developments and applications. Eng Fract Mech 2022;273:108741.
[89] Dundurs J, Tsai KC, Keer LM. Contact between elastic bodies with wavy surfaces. J Elast 1973;3:109–15.